Geochemical and spectroscopic approach to the characterization of earliest cremated human bones from the Levant (PPNB of Kharaysin, Jordan)

Iriarte[1§*], E., García-Tojal[2§], J., Santana[3], J., Jorge-Villar[4], S.E., Teira[5], L., Muñiz[6], J., Ibañez[7], J.J.

[1] *Laboratorio de Evolución Humana, Departamento de Historia, Geografía y Comunicación, Universidad de Burgos, Edifico I+D+i, Plaza Misael Bañuelos, s/n, 09001, Burgos, Spain.*
[2] *Departamento de Química, Universidad de Burgos, Plaza Misael Bañuelos s/n, 0900,1 Burgos, Spain.*
[3] *Department of Archaeology, Durham University, South Road, DH1 3LE, Durham, United Kingdom.*
[4] *Facultad de Educación, Universidad de Burgos, C/ Villadiego, 1, 09001, Burgos, Spain; CENIEH, Paseo Sierra de Atapuerca, 3, 09002, Burgos, Spain.*
[5] *Instituto Internacional de Investigaciones Prehistóricas de Cantabria, Universidad de Cantabria, Avda. de los Castros 52, Edificio Interfacultativo, 39005, Santander, Spain.*
[6] *Pontificia Facultad de San Esteban de Salamanca, Pza. Concilio de Trento s/n, 37001, Salamanca, Spain.*
[7] *Institución Milá y Fontanals, Consejo Superior de Investigaciones Científicas, Egipciacas 15, 08001, Barcelona, Sapin.*

[§]: Both authors contributed equally to this manuscript.

*: Corresponding autor: Dr. Eneko Iriarte (eiriarte@ubu.es).

ABSTRACT:

Cremation is a widespread funerary practice that aims to burn the body and create a new appearance of human remains. It has been interpreted as a ritual transition that includes a sequence of acts and processes aimed at commemorating the dead on an individual and collective scale. In the Near East, fire-induced manipulation or cremation was not a usual burial practice during the Pre-Pottery Neolithic. In this contribution, we present the geochemical (X-ray fluorescence), mineralogical (X-ray Diffraction) and spectroscopic (Raman spectroscopy, Fourier Transform Infrared Spectroscopy and (Electron Paramagnetic Resonance) analysis of bones from a Late Pre-Pottery Neolithic B (*ca.* 9000 yr cal BP) burial in Kharaysin site (Quneya, Zarqa) in northwest Jordan. We discuss the data obtained by the different analytical methods reviewing the state of the art of each analytical method to infer bone burning palaeotemperatures. Finally, it is demonstrated the burned character of the analysed bones, confirming the earliest presence of cremated human bones in a funerary context of the Pre-Pottery Neolithic of the Near East in Kharaysin. This fact provides a new insight into the complexity and variability of burial customs within the Pre-Pottery Neolithic in Levant.

KEYWORDS: Cremation, PPNB, Jordan, X-ray diffraction, FTIR, EPR, Raman Spectroscopy.

1. INTRODUCTON

Cremation it is not just burning bones, it represents a social process that includes a wide range of actions involving burning, the living and the deceased (Goldstein and Meyers 2014; Cerezo-Román et al., 2017). Interpretations define cremation as a ritual transition that includes a sequence of acts and processes aiming to commemorate the dead at an individual and collective scale (e.g. Larsson and Nilsson Stutz, 2014).

Burned bone undergoes a range of significant changes, which have been described and discussed elsewhere (e.g. Uberlaker and Scammell, 1992; Mayne Correia, 1997; Thompson et al., 2009; Gonçalves et al., 2011; Depierre, 2014; Schmidtand and Symes, 2015; Thompson, 2015a; Gonçalves and Pires, 2017; Piga et al., 2016 & 2018), and the nature and degree of which are highly influenced by its heterogeneous nature. Thus, understanding heat-induced changes and interpreting what they mean with regard to the burning context is difficult. In this work we investigate the burned character of human bones in a PPNB burial in Kharaysin archaeological site (Jordan) (Ibañez et al., 2016) (Fig. 1) in order to infer if they evidence the earliest human cremation in the Near East.

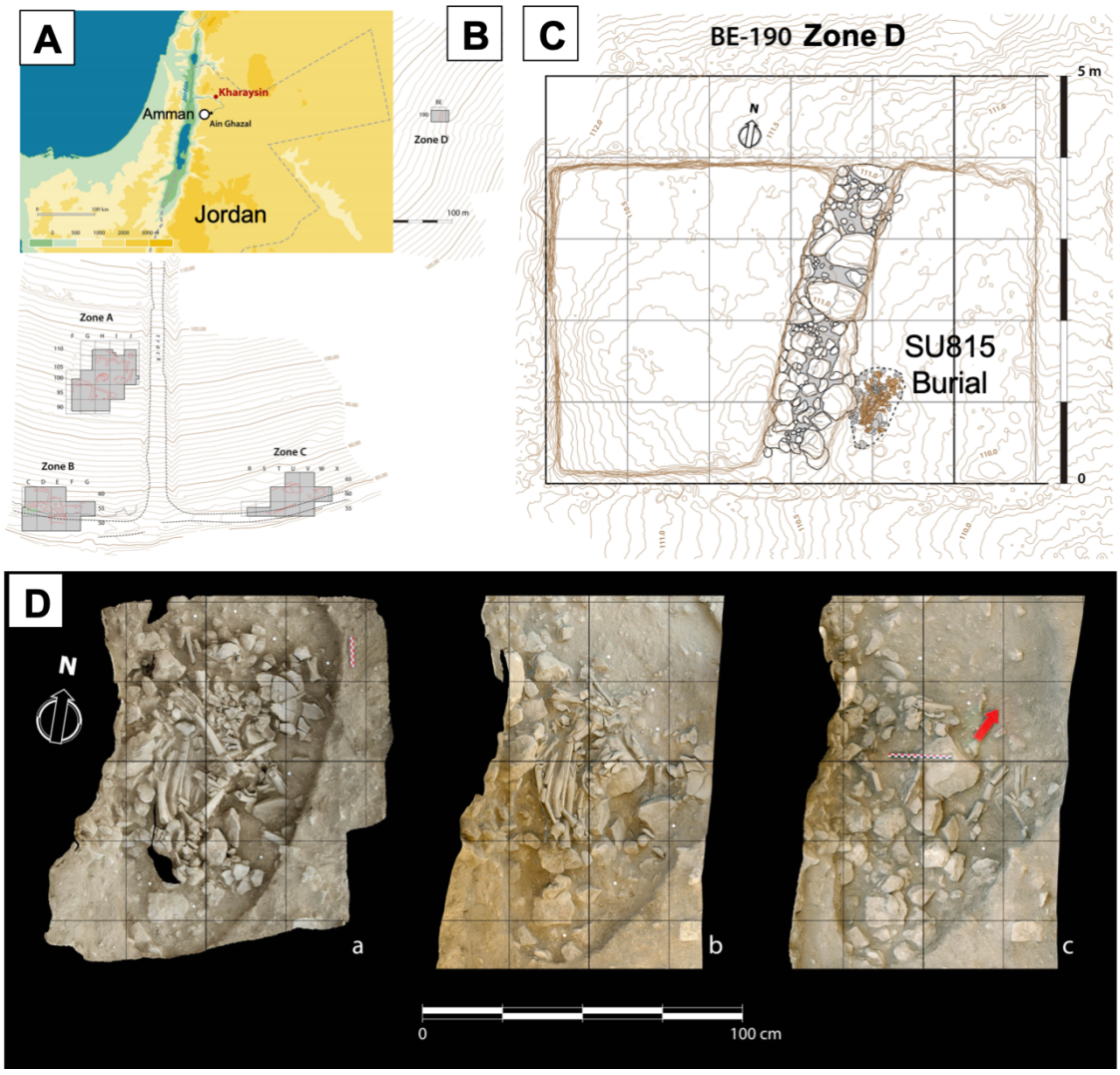

Figure 1. Kharaysin archaeological site. **A)** Geographical location in the Zarqa river valley (NW Jordan). **B)** Map of the excavation areas in Kharaysin site. Note the location of SU815 burial in the northeastern Zone D. **C)** Detailed map of Zone D excavation and SU815 burial. **D)** Photographic sequence of the SU815 burial excavation process.

In the Levant, the earliest cremations known so far come from the Pre-Pottery Neolithic C site of Beisamoun in Israel. At this site, archaeologists have found three cremations: two secondary deposits of selected human remains and a combustion-burial structure with few cremated human bones (Bocquentin et al., 2014). Younger cremations were reported in three Pottery Neolithic sites at the northern Levant: Yarim Tepe II (Merpert and Munchaev, 1993), Yümüktepe (Garstang, 1953), and Tell 'Ain el-Kerkh (Tsuneki, 2011). At Tell 'Ain el-Kerkh, four collective cremation burials were found with at least 37 cremated individuals. Three were in situ cremation pits and multiple burning temperatures were observed on bones. This burial practice was associated with primary and secondary pit burials at the earlier stages of the Pottery Neolithic, but cremations

declined later (Tsuneki, 2011). At Yarim Tepe II and Yümüktepe, secondary and primary cremations were reported. At Yarim Tepe (*ca.* 5800-5400 BC), there is also evidence that some bodies were cremated soon after dead.

The use of analytical data to build sets of indices which allow to evaluate the composition, crystallinity and burning temperatures of bones have been critically reviewed, mainly in the case of X-ray Diffraction (XRD) and Fourier Transform Infrared Spectroscopy (FTIR) studies (Ellingham et al., 2015; Thompson, 2015 a & 2015b; Gonçalves et al., 2018; Mamede et al., 2018b; Monnier et al., 2018; Greiner et al., 2019). One of these indices is the crystallinity index, named CI or, in the case of FTIR studies, also called splitting factor (SF). Despite this parameter has been used for both crystallographic and spectroscopic studies, it is well established that it is not possible to establish a rigorous comparison between the CI values calculated from FTIR to those reached using XRD due to the methodological differences. FTIR is based on an area averaging approach, while XRD deals with a volume averaging method (Thompson et al., 2009). In fact, even for indices obtained from the same technique, as FTIR itself, there are several sources of discrepancy among the different studies: the measurement method (i.e. transmitance *vs.* reflectance), the base line correction performed, the grinding of the sample and particle size, the presence of different elements of mineral phases, etc. Some of these items will be discussed in the present study.

In this contribution, we present the geochemical (X-ray fluorescence), mineralogical (X-ray Diffraction) and spectroscopical (Raman spectroscopy, Fourier Transform Infrared Spectroscopy and Electron Paramagnetic Resonance) analysis of bones from Burial SU815 in Kharaysin site, a secondary multiple burial with bone remains of three individuals. This burial is located in Late Pre-Pottery Neolithic B levels of Kharaysin site (Quneya, Zarqa) in northwest Jordan (Ibañez et al., 2016) (Fig. 1), a bone from the burial has been direct dated at 9007-8774 yr cal BP (Supplementary Information). We discuss the data obtained by the different analytical methods to finally infer the burned character of the analysed bones, confirming the earliest presence of cremated human bones in a funerary context of the Pre-Pottery Neolithic of the Levant in Kharaysin.

2. MATHERIAL & METHODS

2.1. Sampling

Burial SU815 was located in the square BE190 at the northeastern area (Zone D) of Kharaysin PPNA/PPNB archaeological site (Fig. 1). It corresponds to an oval-shaped pit nearby a stone wall. The burial contained an assemblage of 329 commingled and fragmented human remains which were simultaneously disposed. Many of these bones (129 remains) present colour changes attributable to burning. Lack of anatomical coherence and disarticulation indicate the secondary disposal of bones. Moreover, some bones displayed clear traits of fire-induced alterations comprising colour changes and breakage. 13 different black to white coloured bones were selected for analysis (Fig. 2).

The burial included a minimum number of individuals (MNI) of 3, calculated by taking into account body size, age and sex (Buikstra and Ubelaker 1994; Lyman 1994). Postcranial remains suggest a MNI of three individuals by the number of ulna, femur and tibia. Sex was estimated by the morphological appearance of the skull and pelvis (Bruzek 2002; Buikstra and Ubelaker 1994; Coqueugniot and Weaver 2007) indicating the presence of one male, one woman, and one indeterminate. Age was estimated in two individuals according to standard methods (Buikstra and Ubelaker 1994; Cardoso 2008a; Cardoso 2008b), comprising one young adult based on recent fusioned postcranial bones (17-25 years old), and one mature adult according to the appearance of symphysis pubic (30-39 years old). Only two individuals´ bones are afflicted by fire-related colouring/alteration (Fig. 2).

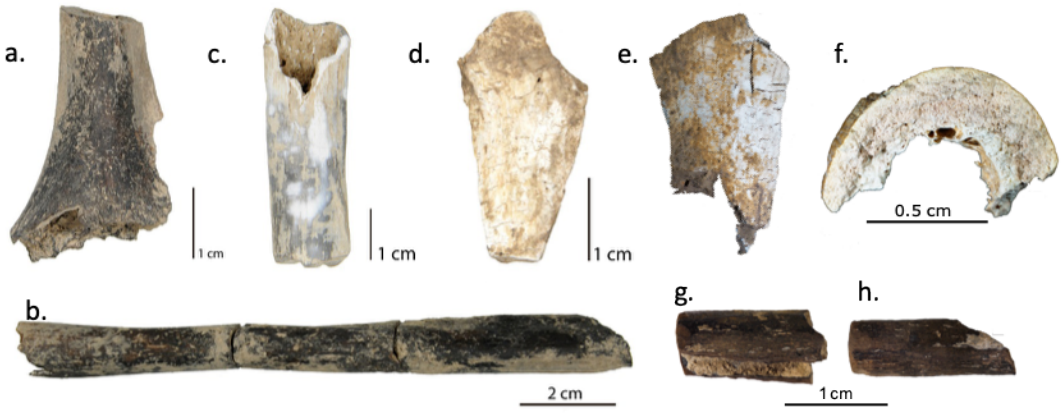

Figure 2. Burnt human remains from the burial SU815; **a. b. g. & h.** Dark-black colour; c. d. & e. Chalky-white colour; **d. & e**. Heat-induced fractures (cracking) in a chalky-white specimen. f. Medieval unburned bone, reference sample (F1). d. e. g. & h. photographs correspond to B1, B2, N1 and N2 samples respectively.

We classified bone colour according to de Becdelievre et al. (2015), where the following bone colours are stated: *yellowish* (107 remains), *brown-grey* (27), *dark-black* (75), *blue-grey* (1), and *chalky-white* (26). In our samples bone remains from 3 main different groups were observed*: dark-black, chalky-white and mixed (*with two or more colours) groups (Fig. 2). Samples from homogeneous *dark-black* and *chalky-white* groups were selected for detailed analysis to infer their burned character and burning

temperature. Two representative samples (N1 and N2) of *dark-black* bone fragments, two samples of *chalky-white* bone fragments (B1 and B2) and a reference medieval unburned bone sample (F1) from the 12th century necropolis of Torrejón (Medina del Campo, Valladolid, Spain) were selected for analysis (Fig. 2). A synthetic hydroxyapatite (HAp) sample was also elaborated following Hayek et al. (1963) (see Supplementary Information) and analysed as reference sample in FTIR and EPR analyses.

2.2. X-ray Diffraction, X-ray Fluorescence and Loss on Ignition organic carbon determination

After carefully dry-cleaned and powdered using an agate mortar, the semi-quantitative X-ray diffraction (XRD) mineralogical analysis of the samples was done using a *Bruker D8 Advance* diffractometer equipped with a Cu tube (voltage 40KV and intensity 30 mA) and a *LynxEye XE* detector. *DIFFRACplus basic EVA* software package was used for the diffractogram interpretation and mineral identification. Two different scan settings were used; the first one consisted in a general scan from 10° to 70° 2θ angles with a step-size of 0,05° and a measuring time per step of 2 seconds. A second scan, focused in the phosphate identification, was done between 32° to 40° 2θ angles with 0.02 step-size and 5 seconds measuring time. Hydroxyapatite crystallinity index (CI) based on the X-ray powder diffractometric pattern of bone carbonate hydroxyapatite was calculated following Person et al. (1995). This CI value provides a semi-quantitative way to estimate the diagenetic changes in archaeological and palaeontological bone phosphate.

An X-Ray Fluorescence (XRF) semi-quantitative geochemical analysis of the samples was also done. The powdered samples were transformed into beads using an *EQUILAB F1 Induction Fluxer* after adding lithium metaborate/tetraborate ($Li_2B_4O_7$) (50% wt.) and potassium bromide (KBr) (0.5 % wt.) fundents. The analyses were performed in a *Thermo ARL ADVAT XP* sequential XRF device. *WinXRF.ADVANT 3.2.1* and *UNIQUANT v.5.47* software packages were used for the data interpretation.

The percentage weight lost on ignition (LOI) was also measured, it gives a crude measure of the organic content of the analysed bones. The dried (14 hours at 110°C) sediment samples in porcelain crucibles were placed in a furnace (*Hobersal HD-230*) and kept at 550°C for 4 hours. When they have cooled, they were re-weighted, and the percentage of the dry weight lost on ignition was then calculated.

2.3. Raman Spectroscopy

Raman analyses were performed using a *DXR confocal Raman Thermo Fisher* spectrometer coupled to an *Olympus* microscope. All samples were analysed using a near-infrared laser operating at 780 nm wavelength, and 1 mW laser power. Accumulations ranged from 40 to 60 at 10 second exposure time.

2.4. Fourier Transform Infrared Spectroscopy

Fourier Transform Infrared Spectroscopy (FTIR) analyses were performed in the medium infrared region (4000-400 cm^{-1}) by a *JASCO FT-IR 4200* spectrophotometer, equipped with an *ATR PRO ONE* single reflection device for attenuated total reflectance (ATR) measurements. Each recorded spectrum is the result of 128 scans at 4 cm^{-1} resolution. The preparation of the synthetic sample of hydroxyapatite $Ca_{10}(PO_4)_6(OH)_2$ for comparative purposes was carried out following a procedure based on the previously reported by Hayek *et al.* (1963) (see Supplementary Information).

2.5. Electron Paramagnetic Resonance

Powdered samples of F1, N1, N2, B1 and B2 bone samples, together with synthetic hydroxyapatite were measured by X-band electron paramagnetic resonance (EPR) with a *Bruker EMX* spectrometer, equipped with a *Bruker ER 036TM* NMR-teslameter and an *Agilent 53150A* microwave frequency counter. In all the measurements, modulation frequency was 100 kHz and modulation amplitude 0.1 mT. *WINEPR SimFonia v1.25* (*Bruker Analytische Messtecnik GmßH*, 1996) program was used to perform the simulated spectra and graphics were carried out with *Kaleidagraph v4.1.1* (*Synergy Software*, 2010) software. At least two measurements per sample were carried out. Experimental details are given in figure captions.

3. RESULTS

3.1. X-ray Diffraction, X-ray Fluorescence and organic matter content (LOI)

X-ray fluorescence analyses (Table I and Figure 3) show the elemental composition of the analysed bone samples (expressed in oxides and % of sample weight). There are not significant changes in major element composition, Ca, P and F (Fig. 3 and Table I). In general, a slight increase in the relative content of some elements as Na, Mg, S and Sr is visible from fresh to dark-black bone samples and a subsequent depletion of the same elements from dark-black to chalky-white bone samples could be inferred (Table I). The organic C content measured (LOI) shows a strong depletion from fresh bone (7% wt.) and dark-black bone (8.5-8% wt.), to chalky-white bone samples (0.9-0,6% wt.) (Table I & Fig. 3).

Table I. XRF elemental geochemical composition, mineralogical composition and organic carbon content of analysed bone samples. Values are expressed in sample weight percentage (% wt). Hydroxyapatite Crystallinity Index was calculated following Person et al. (1995).

Sample	Bone colour	LOI (550ºC)	CaO	P2O5	F	Br	Na2O	MgO	SO3	Al2O3	SiO2	SrO	Hydroxyapatite	Calcite	HAp Cristallinity Index
F1	Yellowish	7.6443	51.64	41.94	2.73	2.15	0.395	0.311	0.251	0.231	0.123	0.0659	100	0	0.54
N1	Dark-black	8.4877	52.40	35.99	0	2.12	1.09	0.833	0.389	0.328	5.88	0.112	80,32	19.68	0,19
N2	Dark-black	7.9574	53.83	38.40	2.13	2.31	1.08	0.797	0.357	0.252	0.334	0.106	89,39	10.61	0.12
B1	Chalky-white	0.3612	50.46	38.60	4.25	3.9	0.836	0.417	0.067	0.364	0.748	0.0259	97,94	2.06	1.24
B2	Chalky-white	0.9019	52.95	40.03	2.08	1.92	0.686	0.413	0.0891	0.275	0.91	0.0245	96,5	3.5	1.26

XRD analysis shows that all bone samples are composed of hydroxyapatite (HAp), but calcite is also present in dark-black (N1 & N2) and chalky-white samples (B1 & B2) (Table I, Fig. 3 & Fig. S1). Unburned Medieval bone is composed of HAp (100% wt.) but dark-black bone samples show variable and relatively high (19.7-10.6% wt.) calcite content. The calcite content is drastically reduced in chalky-white samples (3.5-2% wt.) (Table I, Fig. 3 & Fig. S1).

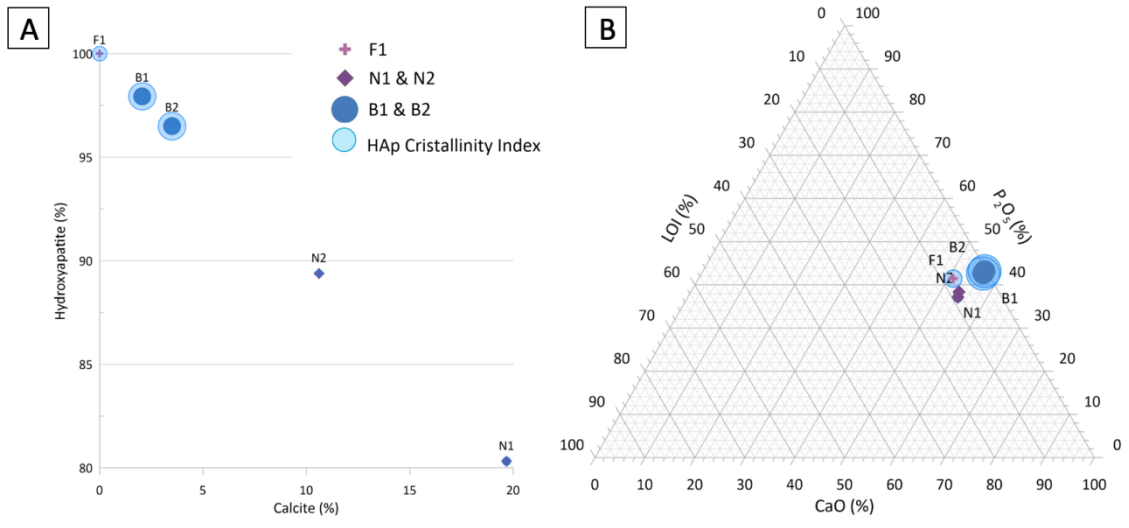

Figure 3. Mineralogical and geochemical data of analysed bone samples. **A)** Bubble diagram showing the variation in major minerals and Hap Crystallinity Index (CI) from the analysed samples. **B)** Ternary diagram representing the major elemental composition differences of analysed samples: medieval unburned bone (F1), dark-black bone (N1 & N2) and chalky-white bone samples (B1 & B2).

Diffractograms from analysed samples (Fig. 4 & Fig. S1) show that no other phosphate mineral phase is present except for the HAp. The only significant difference is related to the HAp peak intensity observed in different samples (Table I, Fig. 4 & Supplementary Information); these intensity variations are related to crystallinity changes (Person et al., 1995; Piga et al., 2013; Greiner et al., 2019). Medieval unburned bone sample shows a relatively high CI value (0.54). However, in the dark-black samples the CI decreases to 0.19 (N1) and 0.13 (N2), being the lowest values of analysed samples (Fig. 3). Finally, the chalky-white bone samples yielded the highest CI values reaching 1.24 (B1) and 1.26 (B2) (Table I, Fig. 4 & Fig. S1).

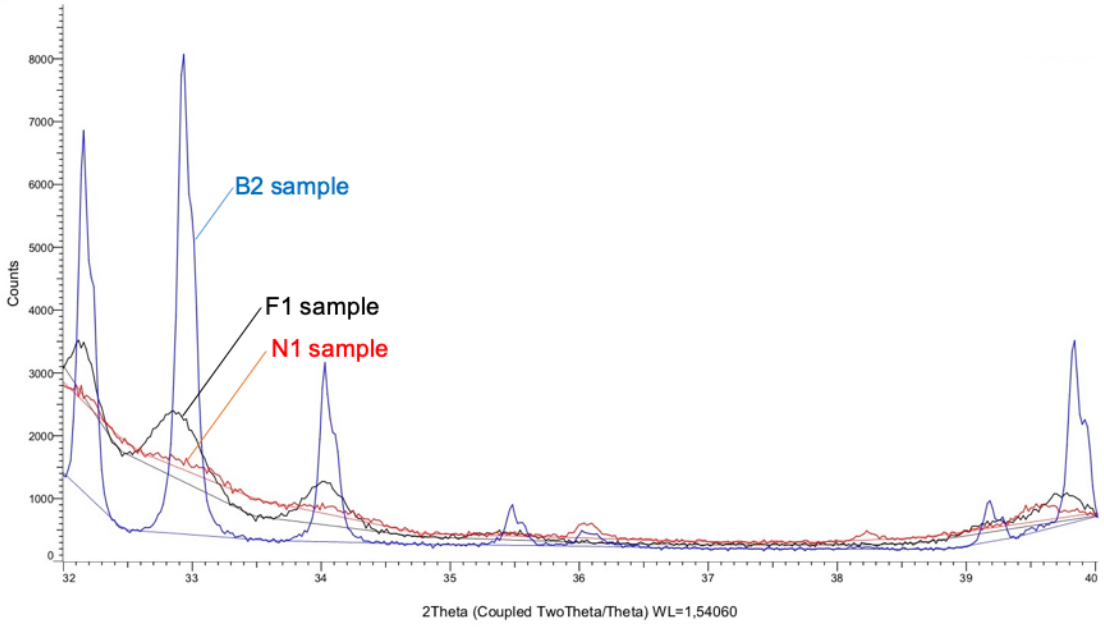

Figure 4. X-ray diffractograms of analysed samples between 32 and 40º 2θ angles showing the intensity peaks related to HAp. Medieval bone sample (F1, black), dark-black bone sample (N1, red) and chalky-white bone sample (B2, blue). Notice the differences in HAp peak intensity.

3.2. Raman spectroscopy

All Raman spectra obtained from analysed samples show very high fluorescence and weak or very weak Raman signatures, which could be related to the presence of organic compounds, which, in our case, is very likely. The main minerals found in the samples were hydroxyapatite, calcite and carbon (Table II & Fig. 5).

The most common signature is located at 962 cm^{-1} and was assigned to the ν_1 symmetric stretching Raman vibration of the PO_4 and related to the presence of hydroxyapatite (Fig. 5). This band appears with very low intensity, for what no other Raman band from lattice modes nor on the O-H stretching bonds appears, except for some spectra from the Medieval unburned bone (F1). In unburned bone, Raman spectra show, together with the signature at 962 cm^{-1}, one weak band at 1072 cm^{-1} related to the ν_4 stretching PO_4 mode and/or to the ν_1 CO_3 stretching mode, and the signatures at 590 and 434 cm^{-1}, that are related to the ν_4 and ν_3 bending modes of PO_4 respectively (Wopenka & Pasteris, 2005; Antonakos et al., 2007). Despite of the absence of weaker bands, the identification of hydroxyapatite in those samples is accepted since any other calcium phosphate shows the PO_4 signature at higher wavenumbers (Edwards et al., 2005) and, furthermore, hydroxyapatite was also identified in this work by using X-ray diffraction and IR spectroscopy.

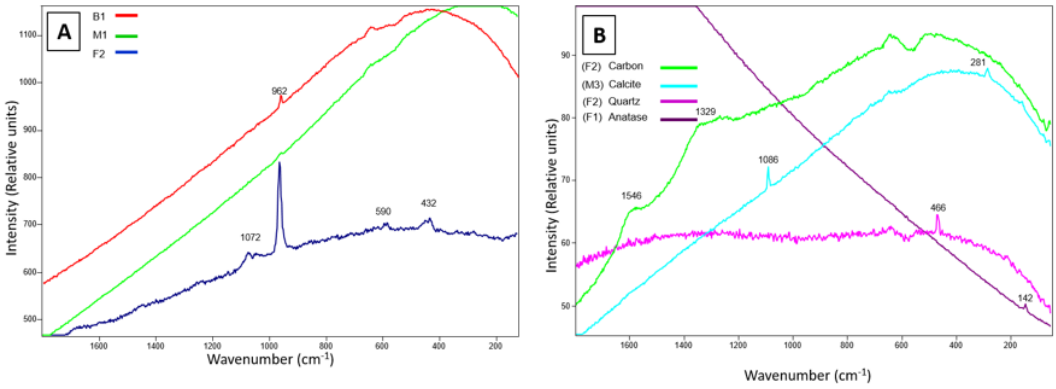

Figure 5. Raman spectra of most significant components from the studied bone samples. **A)** Raman spectra obtained on calcinated, carbonized and not-burned bones. The main phosphate band is visible in all spectra, although in the spectrum of carbonized bone (N1, M1 & M3), the signature is very week; however, on the unburned medieval bone (F1 & F2) other identificative hydroxyapatite bands appear. **B)** Raman spectra of other minerals found on the samples. Carbon and calcite are related to the burnt bone but quartz and anatase are related to adherences of soil and other mineral impurities.

Calcium carbonate was detected in some of the spectra because of the ν_1 symmetric stretching CO_3 vibration at 1086 cm^{-1}; however, only in two of the carbonized and in one of the white-chalky bone sample (B2), the presence of the signature at 281 cm^{-1} (lattice mode) supports the assignment to calcite instead to aragonite (Edwards *et al.,* 2005) (Table II & Fig. 5).

Carbon is another compound identified in most of the samples by the Raman vibrations at around 1329 and 1546 cm^{-1}, related to the D and G modes respectively (Ferrari & Robertson, 2000) (Table II & Fig. 5).

Apart from the previously explained compounds, quartz (466 cm^{-1}), anatase (142 cm^{-1}) and some unidentified minerals, probably clay minerals, were also detected in some samples but they are linked to the diagenetic crust and sediment adherences on the bones.

Table II. Mineral phases detected by Raman Spectroscopy analysis of analysed bone samples.

Samples	Calcium Phosphate Hydroxylapatite (962 cm^{-1})	Calcium Carbonate (1086 cm^{-1})	Carbon (1546, 1329 cm^{-1})	Other minerals
F1	X		X	Anatase, 220 cm^{-1} 1360, 614 cm^{-1}
Dark-Black bone				
M1	X	X		648, 530, 499 cm^{-1}
M2		X		
M3		X (+ 281 cm^{-1} calcite)	X	
M4	X	X (+ 281 cm^{-1} calcite)	X	
N1				
N2*		X	X	
N3*		X		920, 845 cm^{-1}
Chalky-White bone				
B1	X	X	X	652 cm^{-1}
B2	X	X (+ 281 cm^{-1} calcite)		

* The results are not from the bone properly but from white adherences on the surface

3.3. Fourier Transform Infrared Spectroscopy

The infrared spectra of five bone samples are provided in Figure 6 (and Supplementary Information). In addition, synthetic hydroxyapatite has been prepared for comparative purposes, whose spectrum can be seen in Supplementary Information (Fig. S2). In the latter, the absorptions due to proper hydroxyphosphate $Ca_{10}(PO_4)_6(OH)_2$ content can be differenced from variable amounts of carbonate ions incorporated in the structure by replacement processes. The assignments are given in Table III. Briefly, the sharp and weak peak at 3572 cm^{-1} has been attributed to ν(O−H) modes of hydroxyde

OH^- groups (Mamede et al., 2018a; Menzel et al., 1972; Diallo-García et al., 2014) arranged in columns inside the channels parallel to the c axis in the structure of hydroxyapatite (De Leeuw, 2001). The weak bands at 1457 and 1412 cm^{-1} have been assigned to $\nu_3(CO_3^{2-})$ modes of distorted carbonate groups placed inside the hydroxyapatite structure. The intense absorptions at 1087 and 1022 cm^{-1} are due to $\nu_3(PO_4^{3-})$ modes in tetrahedra with C_{3v} symmetry, while the band at 962 cm^{-1} is attributed to $\nu_1(PO_4^{3-})$ vibrations (Mekhemer et al., 2019). The very weak absorption at 879 cm^{-1} is ascribed to $\nu_2(CO_3^{2-})$ modes (LeGeros et al., 1969). The strong peak at 629 cm^{-1} is attributed to libration modes of OH^- groups (Menzel et al., 1972; Drouet et al., 2018). At 599 and 562 cm^{-1} appear very intense absorptions corresponding to $\nu_4(PO_4^{3-})$ vibrations. Finally, the medium intensity band at 473 cm^{-1} seems to be mainly due to $\nu_2(PO_4^{3-})$ modes (Marques et al., 2018).

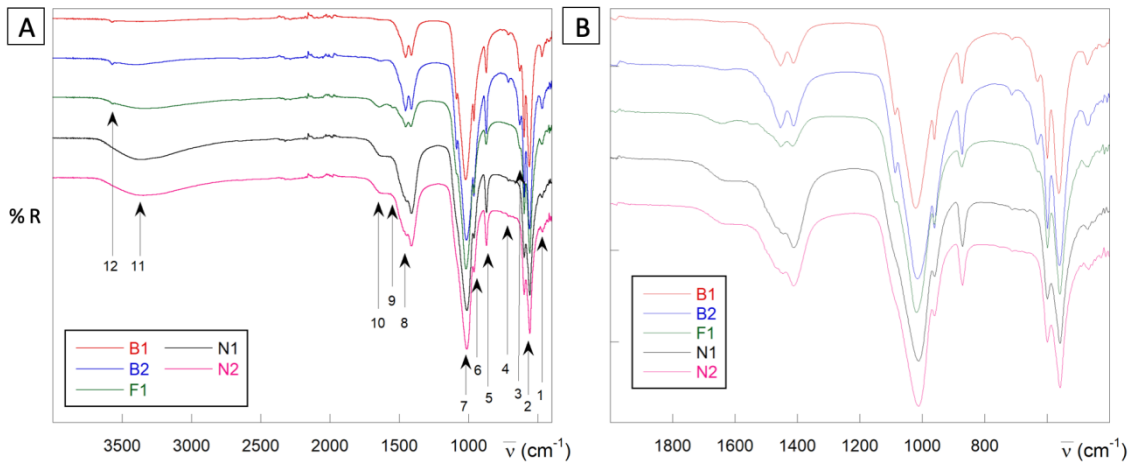

Figure 6. Infrared spectra of analysed bone samples. **A)** Infrared spectra of white-chalky bone samples (B1 in red; B2, blue), unburned Medieval bone sample (F1, green), and dark-black bone samples (N1, black; N2, pink). **B)** Magnification of the 2000−4000 cm^{-1} region. For the assignments related with the numbers given to the bands in Figure A, see Table III.

Table III. Selected IR bands (cm^{-1}) and assignments for synthetic hydoxyapatite and all the measured samples of bones. Main labels: sharp, sh (shoulder), v (very), s (strong), m (medium), w (weak). The numbers in brackets given in the Assignments column correspond to the labels of the bands in Figure 6.

HA	F1	N1	N2	B1	B2	Assignments
3572 w	3571 vw			3572 vw	3572 vw	$\nu(O-H)_{HA}$ (12)
	3332 vb,w	3365 vb,m	3348 vb,m		3402 b,w	$\nu(OH)_{water}$ / ν(NH) (11)
	1644 w	1630 vb,m	1630 vb,m		1633 vw	δ(HOH) + Amide I (10)
	1547 w	1600 vb,m	1600 vb,m			Amide II / $\nu_3(CO_3^{2-})$ (9)
1457 vw 1412 vw	1454 m 1416 m	1445sh,s 1411 s	1445sh,s 1411 s	1455 m 1412 m	1455 m 1412 m	$\nu_3(CO_3^{2-})$ (8)
1087 s 1022 vs	1084 sh,s 1018 vs	1080 sh,s 1012 vs	1080 sh,s 1012 vs	1087 s 1021 vs	1087 s 1014 vs	$\nu_3(PO_4^{3-})$ (7)
962 s	961s	961s	961s	961s	961s	$\nu_1(PO_4^{3-})$ (6)
879 vw	873 m	871 s	872 s	873 s	872 s	$\nu_2(CO_3^{2-})$ (5)
		712 vvw	712 vvw	713 vw	713 vw	$\nu_4(CO_3^{2-})$ (4)
629 s	629 sh,m			631 m	631 m	$\nu_{libration}$(OH) (3)
599 s 562 vs	599 s 559 vs	599 s 559 vs	599 s 559 vs	599 s 562 vs	599 s 560 vs	$\nu_4(PO_4^{3-})$ (2)
473 m	474 w 467 w	470 vw	467 vw	471w	470 w	$\nu_2(PO_4^{3-})$ (1)

Regarding the bone samples, the spectra of the white calcined samples B1 and B2 are essentially the same (Fig. S2 & Table III). The comparison with the spectrum of synthetic hydroxyapatite (Fig. S3) evidences strong analogies, but the bones exhibit a greater carbonate content (see bands around 1455, 1412 and 873 cm^{-1}). B2 also shows the presence of water (weak bands at 3402 and 1633 cm^{-1}), which is negligible for B1

and synthetic sample. Besides, a weak band at 713 cm^{-1} is observed in B1 and B2, which is absent in the synthetic hydroxyapatite. Bands around 700 cm^{-1} in burned bones have been previously reported (Reidsma et al., 2016), being attributed in some cases to cyanamide ($N=C=N^{-}$) arisen from the presence of ammonia, which could come from the thermal treatment of protein-containing biological materials (collagen, skin, etc.) (Snoeck et al., 2014). However, in these publications, the band at 700 cm^{-1} is concomitant with another one quite more intense at 2010 cm^{-1}, which is absent in our spectra. This fact, together with the high temperature of the thermal treatment necessary to calcine the bone samples, allow us to propose this band as a result of $\nu_4(CO_3^{2-})$ modes (Marques et al., 2018; Almança Lopes et al., 2018). Some authors relate this band with the presence of calcite in the bone (Scorrano et al., 2017).

Slight divergences affecting the carbonate modes in B1 and B2 could be ascribed to the different kind of replacement in the analysed bonds respect to the synthetic compound. In this respect, carbonate ions can incorporate into the channels parallel to the c axis by substitutution of hydroxyde OH^{-} anions (type A carbonate) or inside the phosphate arrangement by replacement of PO_4^{3-} groups (type B carbonate) (Rey et al., 1989; Lee Thorp and Sponheimer, 1999; Marques et al., 2018). Type A carbonates use to exhibit bands at 1545 and 1450 cm^{-1} (ν_3) together with a unique signal in the 878−881 cm^{-1} region (ν_2). Type B carbonates show absorptions about 1465, 1412 cm^{-1} (ν_3) and a single band in the 870−873 cm^{-1} range (ν_2) (Fleet, 2009). The values of the energies would suggest the presence of a predominant amount of type B carbonate (873 cm^{-1}) in the bone samples. Anyway, a magnification of the region related with ν_2 (Fig. S5) shows that bands are not symmetric because unresolved shoulders appear at wavenumbers close to 878 cm^{-1}, and the envelopes could obscure absorptions generated by both A and B sites. The same problem arises in the 1400−1500 cm^{-1} region. Anyway, the predominance of B carbonate ions seems to be clear for all the bone samples. However, the low carbonate content in the synthetic hydroxyapatite precludes any clear conclusion about A and B sites in the compound prepared in the laboratory, which would explain the apparent disagreement between the presence of a very weak band around 879 cm^{-1}, while no band at 1545 cm^{-1} is clearly observed.

The Medieval unburned bone sample (F1) contains all the features described for B1 and B2 (Fig. 6 & Table III), together with weak bands of water probably overlapped with absorptions of collagen (Schmidt et al., 2017) at 3330 ν(NH), 1644 (Amide I) and

1546 (Amide II) cm^{-1}. Taking into account the discussion on the A and B position for carbonate ions given above, we cannot discard the band at 1546 cm^{-1} as due, at least in part, to carbonate type A. In this sense, note that F1sample exhibits the less marked predominance of the 873 cm^{-1} minimum of all the bone samples (Fig. S5). Finally, no band at 713 cm^{-1} is observed in F1.

On the other hand, spectra of N1 and N2 are nearly identical and exhibit resemblances with those previously mentioned. Some features deserve to be mentioned in them, as the absence of hydroxide stretching and libration bands around 3570 and 630 cm^{-1}, respectively, together with the presence of higher amounts of water and organic matter (broad bands around 3365−3345 cm^{-1} and a plateau in the 1530−1630 cm^{-1} region), the shift of the band at 1455 to 1445 cm^{-1}, the decrease in intensity of this band with respect to that at 1411 cm^{-1}, and the nearly negligible absorptions at 713 cm^{-1}.

3.4. Electron Paramagnetic Resonance

The X-band EPR spectra measured at room temperature on powdered samples of F1, N1, N2, B1 and B2 in the 0–700 mT range are given in Figure 7. All of them depict a series of spectra recorded in the same experimental conditions to directly evidence the difference in intensities. F1 is nearly EPR-silent, with an extremely weak signal at g ≈ 4.2. N1 shows a spectrum of low intensity constituted by a broad absorption at $g \approx 12.5$ (band width, $\Delta H = 50.0$ mT), a weak one at $g \approx 4.2$ ($\Delta H = 10.0$ mT), a very broad and complex band at $g \approx 2$ ($\Delta H \approx 80.0$ mT), which is really the envelope of several broad signals, probably including unresolved hyperfine structure and, finally, a thin absorption characteristic of radical species, whose better fit is achieved with a Lorentzian orthorhombic fit $g_1 = 2.0056$ ($\Delta H_1 = 0.3$ mT), $g_2 = 2.0040$ ($\Delta H_2 = 0.3$ mT) and $g_3 = 2.0023$ ($\Delta H_3 = 0.2$ mT) (Fig. S7), in spite of a isotropic one with $g = 2.0040$ ($\Delta H = 0.5$ mT, Gaussian) is also possible (Fig. S7). N2 exhibits a quite similar spectrum, except for the lack of the band at $g \approx 12.5$ and the slight shift in the radical signal, $g_1 = 2.0056$ ($\Delta H_1 = 0.3$ mT), $g_2 = 2.0036$ ($\Delta H_2 = 0.3$ mT) and $g_3 = 2.0025$ ($\Delta H_3 = 0.3$ mT), or isotropic fit with $g = 2.0039$ ($\Delta H = 0.5$ mT, Gaussian).

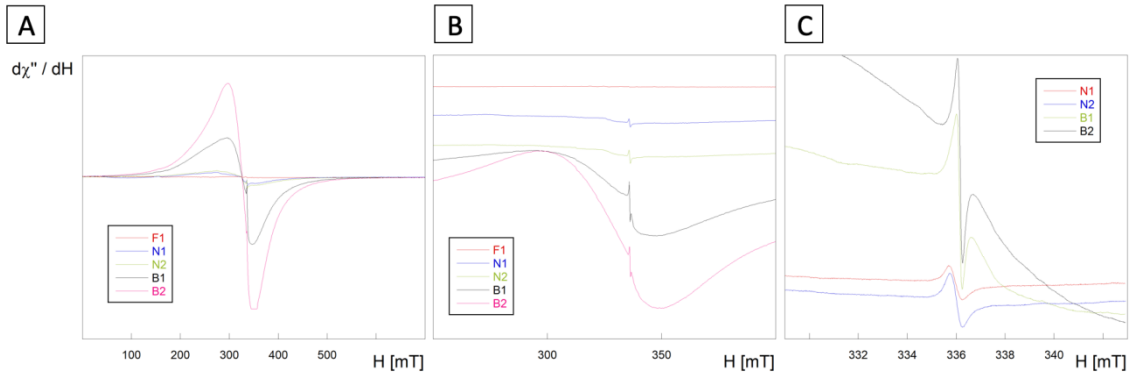

Figure 7. EPR spectra of bone samples. **A)** EPR spectra in the 0–700 mT range. Note that in the experimental conditions, the signal of B2 saturates. Experimental details: modulation amplitude 0.1 mT, time constant 81.92 ms, conversion time 327.68 ms, gain 6.32 10^4 and power 20 mW in all cases. Microwave frequencies: 9.4244 (F1), 9.4239 (N1), 9.4240 (N2), 9.4234 (B1) and 9.4238 GHz (B2). **B)** EPR spectra of bone samples in the 250–400 mT range. Microwave frequencies: 9.4244 (F1), 9.4239 (N1), 9.4239 (N2), 9.4223 (B1) and 9.4237 GHz (B2). **C)** Detail of EPR spectra of bone samples in the 329 – 343 mT range. Microwave frequencies: 9.4220 (F1), 9.4239 (N1), 9.4239 (N2), 9.4234 (B1) and 9.4238 GHz (B2).

The spectrum of B1 exhibits a very large and broad signal at $g \approx 2$, which could be formed through overlapping of two or more broad bands, together with a radical at $g = 2.0030$ ($\Delta H = 0.2$ mT). In the case of B2, the spectrum is analogous, with slight variation in the position of the radical, $g = 2.0029$ ($\Delta H = 0.2$ mT). A comparison between both spectra is given in Figure S8. Both signals are absent in the spectrum of the hydroxyapatite synthesized at 800 ºC (Fig. S9).

No new signals are detected on lowering the microwave power from 20.0 mW to 2.0 and 0.2 mW. However, variations in the width and shape of the radical signal are observed at lower power. On the other hand, the peak-to-peak amplitude has been compared for the broad band around $g \approx 2$ and the radical signal. Regarding the radical, the sequence is:

$$I_{B2} (6\ I_{N1}) > I_{B1} (5\ I_{N1}) > I_{N2} (2\ I_{N1}) > I_{N1}$$

While, in the case of the $g \approx 2$ broad band, the ratios are:

$$I_{B2} (20\ I_{N1}) > I_{B1} (10\ I_{N1}) > I_{N2} (2\ I_{N1}) > I_{N1}$$

4. DISCUSSION

The different analytical methods performed to ascertain the burnt character of studied bone samples has proven satisfactory. However, each analytical methodology shows different results focused in different aspects of the physio-chemical transformations produced during bone burning. In this section the main outcomes from different methodologies and a general assessment of the results are discussed.

4.1. Colouring, mineralogical and geochemical transformations of burned bones

Many studies have demonstrated that colour change is a reliable indicator of different intensity burning of bone remains (Shipman et al., 1984; Devlin and Herrmann, 2008; Greiner et al., 2019). Experimental research indicates the relationship between colour and temperature, as colour change reflects the sequential decomposition of the organic and inorganic components with increasing temperature (Buikstra and Swegle, 1989; Mayne Correia, 1997; Shipman et al., 1984; Stiner et al., 1995). Most scholars agree that yellowish colours form at temperatures from 0 to 200/300 °C; dark brown and black colours from 200/300 °C to 550 °C; greyish colours from 300 to 700 °C, and whitish colours from 600 to 1000 °C (Nicholson 1993; Shipman et al., 1984; Stiner et al., 1995; Symes, 1996; Thompson, 2015b; Walker et al. 2008). Our analytical work supports the colour-based interpretations, and as discussed below, additional FTIR and EPR analyses could help to infer more precisely the burning temperature.

Bone's crystal structure changes fundamentally when heated. Research consistently shows that as the temperature of burning increases, the hydroxyapatite transforms into a purer form, with higher levels of crystallinity, larger crystal sizes overall and reduced porosity (Figueiredo et al., 2010; Thompson, 2015b). This all coincides with the release of the lattice carbonate and water from the bone (Wang et al., 2010). It has been argued that during burning, the crystals become bigger spheroids and that intercrystalline space is simultaneously lost (Hummel et al., 1988). The chemical nature of the bone can change, and studies have detected the presence of new crystal phases within the bone following burning, including β-tricalcium phosphate and $NaCaPO_4$ (Etok et al., 2007; Piga et al., 2018).

Mineralogical and geochemical composition of bones show some changes in analysed bone samples. XRD and RS analyses show that the main mineralogical phase in all the samples is HAp and no new phosphate mineral formation is observed (e.g. whitlockite) indicating that burning temperature in analysed samples did not exceeded >750 ºC for a long time (Piga et al., 2008 & 2013; Monge et al., 2014) (Table I). The

most outstanding mineral change corresponds to the formation of calcite in the HAp, mainly type B carbonate (Fleet, 2009), in dark-black (N1 & N2) samples reaching 19-10 % wt. that sharply decreases in chalky-white samples to 2-3 % wt. (B1 & B2) due to calcination of carbonate (decarbonatation) at temperatures usually higher than 775 ºC (Piga et al., 2008) (Fig. 3 & Table I).

As seen in previous works (e.g. Subira and Malgosa, 1993) there are not significant changes in major and minor element content (Fig. 3 & Table I). The organic C content (LOI) shows the most important change consisting in a strong depletion from fresh (7% wt.) and dark-black bone (8.5-8% wt.), with similar values, to chalky-white bone samples (0.9-0,6% wt.). This fact is due to organic matter combustion during burning; higher temperature and/or burning time involve a higher organic carbon lose as seen in chalky-white samples (B1 & B2). The decrease of organic matter content when crystallinity increases is a typical phenomenon seen in other studies (Person et al., 1995; Thompson, 2015b; Piga et al., 2013 & 2018).

The study of burned bone using crystallinity measures has revealed useful in many archaeological contexts (e.g. Butler and Dawson, 2013; Olsen et al., 2013; Schiegl et al., 2003, Piga et al., 2016a & 2016b). In our case study, mineralogical composition of bones shows that the main mineralogical phase in all the samples is HAp and its crystallinity increases from unburned to white-chalky samples, indicating an increasing burning temperature (Thompson, 2015b; Piga et al., 2008; Greiner et al., 2019). Noteworthy, the most significant structural changes in the bone crystalline phase occur between 500°C and 700°C (Etok et al., 2007, p. 9812) coinciding with the major CI change observed between analysed dark-black samples (N1 & N2) and chalky-white samples (B1 & B2).

4.2. Burning indices and temperature

The FTIR pattern of the spectrum of F1 strongly resembles to that corresponding to unburned bone that has been chemically defatted, deproteinated and dehydrated (Marques et al., 2016; Piga et al., 2010b), but is also similar to the Henry VII's bones spectrum (Scorrano et al., 2017), and even spectra of modern bones heated around 600 ºC (Marques et al., 2018; Gonçalves et al., 2018; Mamede et al., 2018a & 2018b, Thompson et al., 2009; Walker et al., 2016; Piga et al., 2016). The spectra of B1 and B2 agree well with those reported for bones heated in the 700−800 ºC range, which exhibit a good resolution of the bands at 1090−1010, 961 and 631 cm^{-1}, attributed to $\nu_3(PO_4^{3-})$,

474 $\nu_1(PO_4^{3-})$ and $\nu(OH)_{libration}$, respectively (Marques et al., 2018; Gonçalves et al., 2018;
475 Mamede et al., 2018b).
476 The FTIR spectra of N1 and N2 suggest, as a whole, that N1 and N2 are formed
477 as a result of uncompleted pyrolytic processes where water and notable amounts of
478 organic materials remain, as the dark colour denotes. The FTIR spectra of N1 and N2
479 reveal higher organic and water content and lower relative phosphate amount than any
480 other of the measured samples. On the other hand, a spectrum close to those of N1 and
481 N2 is that reported for Reidsma *et al.* (2016) after heating a bone at 340 ºC in reducing
482 conditions, with strong similarities in the absorptions inside the 1400−1630 cm^{-1} region
483 and the lack of hydroxide bands at 3570 and 630 cm^{-1}. In the same way, analogies are
484 observed with other reported results (Schiegl et al., 2003) mainly for thermal treatments
485 below 500 ºC (Marques et al., 2018; Gonçalves et al., 2018; Mamede et al., 2018b).
486 We have selected a set of IR indices for analyzing the samples in order to attain
487 information about the composition and crystallinity, with the aim of deducing the
488 maximum burning temperatures experienced by the bones: i) the splitting factor (SF) or
489 crystallinity index (CI) (Weiner and Bar-Yosef, 1990), which measures the peak
490 sharpening by calculating the quotient of the addition of intensities of the bands about
491 599 and 560 cm^{-1} and the valley at 588 cm^{-1} in Equation 1, over a baseline correction
492 drawn from 750 to 450 cm^{-1}; ii) the amount of type B carbonates with respect to the
493 phosphate content has been evaluated in two different ways, named as BPI (Sponheimer
494 and Thorp, 1999) and B2PI (Piga el al., 2015); iii) the ratio between the whole carbonate
495 content and the type B carbonate (C/C) (Snoeck et al., 2014); and iv) the ratio (OH/P),
496 that relates the amounts of hydroxyde OH^- with the phosphate content through the
497 comparison of the intensities of the libration (630 cm^{-1}) or stretching modes (3572 cm^{-1})
498 of the hydroxyapatite hydroxyde groups and the $\nu_4(PO_4^{3-})$ vibration, OHl/P and OHs/P
499 values, respectively (Snoeck and Schulting, 2014; Ellingham et al., 2015, Mamede et al.,
500 2018a). The corresponding equations are given below (Equations 1−6), and the results
501 are summarized in Table IV. Calculation of BPI, C/C and OH/P are problematic in the
502 carbonized N1 and N2, where the hydroxide bands are not observed and the absorptions
503 of probable organic nature obscure those of carbonates above 1400 cm^{-1} and preclude
504 reliable values for the C/C index. In these cases, the use of the band around 880–870
505 cm^{-1}, corresponding to $\nu_2(CO_3^{2-})$ vibrations, could be more realistic, as it has been
506 pointed out by other authors (Fleet, 2009). Therefore, we have not evaluated the

hydroxide content in N1 and N2, while the carbonates have been analysed by the definition of two new indices (named as B3PI and CB/CA), which have been calculated by using the values of absorbances at fixed wavenumbers (i.e. 880 and 871 cm^{-1} for A and B carbonate types, respectively, equations 7 and 8). Finally, the possible presence of calcite in the most of our samples (band at 713 cm^{-1}), which agree well with interpretation given for other authors to the same spectral motif (Scorrano et al., 2017; Monge et al., 2014), could affect to the bands around 1415 and 870 cm^{-1} because in the $\nu_3(CO_3^{2-})$ and $\nu_2(CO_3^{2-})$ modes in this mineral appear in the same regions. Absorbances of $\nu_2(CO_3^{2-})$ in synthetic hydroxyapatites are negligible, so that B3PI and CB/CA have not been provided for them. Most of calculations have been carried out after correcting the base line, as it is shown in Figures S6 for the F1 sample, considering 750–450, 895–835 and 1590–1300 cm^{-1} regions. In these regions, base line corrections have been performed fitting to zero the absorbance of the extremes, i.e. the absorbance at 750, 450, 895, 835, 1590 and 1300 cm^{-1}, respectively (Figure S6). On the contrary, Equations 3 and 6 lack of base line correction and values are directly read on the absorbance spectra.

$$CI = \frac{A_{599cm^{-1}} + A_{560cm^{-1}}}{A_{588cm^{-1}}} \quad \text{Equation 1}$$

$$BPI = \frac{A_{1415cm^{-1}}}{A_{599cm^{-1}}} \quad \text{Equation 2}$$

$$B2PI = \frac{A_{1415cm^{-1}}}{A_{1035cm^{-1}}} \quad \text{Equation 3}$$

$$C/C = \frac{A_{1455cm^{-1}}}{A_{1415cm^{-1}}} \quad \text{Equation 4}$$

$$OHl/P = \frac{A_{630cm^{-1}}}{A_{599cm^{-1}}} \quad \text{Equation 5}$$

$$OHs/P = \frac{A_{3572cm^{-1}}}{A_{599cm^{-1}}} \quad \text{Equation 6}$$

$$B3PI = \frac{A_{871cm^{-1}}}{A_{599cm^{-1}}} \quad \text{Equation 7}$$

$$CB/CA = \frac{A_{871cm^{-1}}}{A_{880cm^{-1}}} \quad \text{Equation 8}$$

Data point to the calcined B1 and B2 bones, together with the unburned Medieval one (F1), as the most crystalline samples, as shown by XRD CI. Both, BPI, B2PI and

B3PI indices suggest that the carbonized N1 and N2 samples are the richest in carbonate content, followed by the calcined bones. In this sense, carbonate ions are mainly present as type B, above all in both the N1 and N2 samples. F1 could contain the greatest amount of type A carbonate.

Table IV. Calculated burning indices for samples B1, B2, F1, N1 and N2, together with two synthetic hydroxyapatite compounds, HAp_1 and Hap_2. Each value is an average of three independent measurements. Standard deviations are given in parentheses.

Sample	CI	BPI	B2PI	C/C	OHI/P	OHs/P	B3PI	CB/CA
B1	5.3(1)	0.24(1)	0.13(1)	1.09(1)	0.28(1)	0.022(1)	0.220(6)	1.62(4)
B2	5.3(1)	0.26(1)	0.14(1)	1.06(1)	0.29(1)	0.027(2)	0.247(3)	1.67(2)
F1	4.9(4)	0.20(1)	0.10(2)	1.01(1)	0.18(1)	0.035(2)	0.142(6)	1.46(3)
N1	3.8(2)	0.56(1)	0.27(4)	0.74(5)			0.391(11)	1.87(4)
N2	3.8(1)	0.54(1)	0.25(1)	0.78(1)			0.348(4)	1.81(1)
HAp_1	7.8(5)	0.02(1)	0.01(1)	1.03(1)	0.59(3)	0.033(5)		
HAp_2	8.1(7)	0.02(1)	0.01(1)	1.17(1)	0.58(1)	0.038(1)		

The CI values show a qualitative agreement with those calculated by XRD analysis and some of them agree well with those previously published (Gonçalves et al., 2018; Piga et al., 2015; Schiegl et al., 2003; Squires et al., 2011; Thompson et al., 2013). However, other reported works exhibit divergences with our results, in particular lower values for CI and other indices (Scorrano et al., 2017; Mamede et al., 2018a; Stiner et al., 1995; Munro et al., 2007; Piga et al., 2010a; Piga et al., 2016b; Piga et al., 2016).

Seeking into the sources of such discrepancies, it has been demonstrated that transmitance FTIR measurements on KBr pellets give rise to CI indices smaller than those deduced from the ATR technique (Thompson et al., 2009), which is in good accordance with our results because KBr method has been used in some of the above mentioned papers (Munro et al., 2007; Piga et al., 2010a; Piga et al., 2016b; Kontopulos et al., 2018).

Apart from this, as Table S1 summarizes, the CI values strongly depend on the different base-line corrections considered. A correct choice of the background is crucial in order to avoid discrepancies (Gonçalves et al., 2018).

In addition, it has been studied the influence of the grinding and the particle size on the crystallinity and the contact between powdered bone samples and the prism of the equipment and, therefore, in the penetration of the IR beam of light. In this sense, CI increases with decreasing the particle sizes from > 500 μm to 20 – 63 μm (Kontopulos et al., 2018). However, down to 20 – 63 μm particles lose crystallinity and CI decreases (Surovell and Stiner, 2001). This fact could be also related with the differences observed in parameters of the two synthetic HAp samples described in the present work.

Furthermore, Thompson *et al.* (2011) have reported that the addition of fluorine increases CI by promoting the crystal growth. Regarding with this, it has been proposed the presence of a band or shoulder about 1087 cm^{-1} as an indicator of the presence of francolite (fluoroapatite), and even that the $I_{605\ cm^{-1}}$ / $I_{565\ cm^{-1}}$ ratio increases with the degree of fluoridation (Nagy et al., 2008). In our case, the fluorine contents are not quite different and seem not to follow a clear trend with the CI values.

Other possible influence for the disagreement among the results of different studies is the presence of different mineral phases in the samples, mainly different phosphate compounds or calcite. Thus, the appearance of whitlockite, or the synthetic analogous β-tricalcium phosphate, β-$Ca_3(PO_4)_2$, has been interpreted as an effect of heating in the 550 – 1000 ºC range (Monge et al., 2014). It has been discussed about the influence of the presence of whitlockite in the CI values (Piga et al., 2018). In our samples, however, no shoulders around 1123 cm^{-1} not distortions in the bands around 560 cm^{-1} are observed, which suggests that no appreciable amounts of β-$Ca_3(PO_4)_2$ are present. Notwithstanding, a greater phosphate-content in B2 is suggested by the values of BPI and B3PI, in good agreement with the XRF analysis.

On the other hand, the presence of calcite in bones can be included within the diagenetic processes. Calcite is derived from the secondary precipitation of carbonate, typical of any karst system and calcareous soil with alternation of wet and dry periods (Monge et al., 2014). Some authors state that highly carbonated samples exhibit low CI indices (Nagy et al., 2008). Carbonate content uses to decrease drastically from 500 to 600 ºC, temperatures at which the carbonate apatite (bioapatite or dahllite) begins to transform into hydroxyapatite, disappearing at 950 ºC (Lebon et al., 2008). Actually,

588 while $\nu_2(CO_3^{2-})$ and $\nu_3(CO_3^{2-})$ vibration modes of calcite overlap with those of carbonate
589 ions in the bioapatite crystal structures, the band at 713 cm^{-1} attributed to $\nu_4(CO_3^{2-})$ is
590 characteristic of calcite. Because of this, the presence of calcite arising in archaeological
591 bones from precipitation of secondary mineral phases in bone micropores during
592 diagenesis can be monitorized, despite the detection limit of calcite in FTIR ATR
593 measurements is close to 2.5 % since this band is difficult to see at lower calcite contents
594 (Dal Sasso et al., 2016).
595 Our calculations evidence an unusually high CI value for the medieval bone (F1).
596 It is worth noting that diagenetic changes experienced by buried bones may have had an
597 impact on subsequent heat-induced changes (Gonçalves et al., 2018). In fact, the
598 crystallinity appears to increase as a function of diagenetic processes and/or heat
599 treatment (Piga et al., 2016a). Thus, recrystallization of buried bones can take place (i)
600 for many years, as a part of a fossilization process, (ii) as rapid transformations by
601 weathering over few months or decades, (iii) nearly instantaneous by high temperature
602 diagenesis, especially above 650 ºC, and (iv) by bioturbation effects on bones (Stiner et
603 al., 2001; Kontopoulos et al. 2019). Hypotheses (ii) and (iv) could explain, at least in part,
604 the anomalous CI value in F1.
605 A clearer insight can be obtained when more than one index is considered, being
606 the most frequently used the combination of CI and C/P indices (Gonçalves et al., 2018;
607 Piga et al., 2015; Thompson et al., 2013; Squires et al., 2011; Nagy et al., 2008; Koon et
608 al., 2003). In fact, the CI and B2PI values for the medieval unburned F1 bone are close
609 to those reported by Dal Sasso et al. (2016) in meroitic unburned bones (250 – 50 years
610 BCE) from the archaeological site of Al Khiday 2 (in central Sudan). These results were
611 attributed to differences in the diagenetic alteration due to the influence of
612 palaeoenvironmental conditions and climatic changes at regional level.
613 Finally, some authors have related the white colours in bones and B2PI values lower than
614 0.15 with the presence of visible bone cracks (Olsen et al., 2008).
615 All these observations prompt us to give qualitative validity to the results here
616 reported. The absence of OH^- bands for N1 and N2, the values of different indices,
617 together with the spectra profile as a whole, suggest temperatures of carbonization of
618 300−500 ºC for both samples. On the contrary, the thermal treatments in B1 and B2,
619 whose spectra exhibit a clear band at 631 cm^{-1} and the highest OH/P ratios and CI indices,
620 could be in the 700−800 ºC range.

Concerning the EPR analyses, the bands at $g \approx 12.5$ (broad, i), $g \approx 4.2$ (ii) and $g \approx 2$ (very broad, iii) are characteristic of the presence of S = 5/2 ions, mainly high spin Fe(III) ions, in magnetically coupled systems (i), distorted orthorhombic symmetries (ii), and octahedral environments and/or superparamagnetic iron nanoparticles (iii), respectively (Pon-On et al., 2007; Bertolino et al., 2010). As in our case, it has been reported variations in the width of these bands with temperature for ceramic carbonate-rich objects (Ionescu et al., 2014). These absorptions can affect the radical signal. As a whole, their intensities could suggest two possibilities, (i) the iron content is greater in the white calcined samples and follows the trend B2 > B1 > N2 > N1, or/and (ii) the burning process originates magnetic changes in iron-containing minerals. Taking into account the XRF measurements, the latter seems the most probable possibility. If this hypothesis is right, an increment in the intensity of the broad EPR signal could correspond to transformation / formation of magnetic minerals as a result of the thermal treatment. In this regard, dehydration processes at ~ 280 ºC, transformation of maghemite into magnetite and hematite (~ 400 ºC) and formation of secondary magnetite over 500 ºC have been reported (Kostadinova-Avramova et al., 2013; Carrancho et al., 2016; Tema and Ferrara, 2019). Therefore, the presence of low intensity signals would suggest temperatures lower than 400 ºC for the carbonized N samples.

The radical signal shifts to lower *g*-values from 2.0040 in carbonized to 2.0030 in calcined samples and its line width narrows, from 0.5 to 0.2 mT, while the peak-to-peak amplitude increases. Taking into account the experimental error ±0.0007, this signal could be that reported at $g = 2.0046$ attributed to organic radicals for most of authors (Ikeya, 1993; Dennison and Peake, 1992; Oduwole et al., 1993; Walker et al., 2016) or to CO^- radical anions (note, in this case, the values reported by Callens et al., (1998), $g_x = 2.0057$, $g_y = 2.0043$ and $g_z = 2.0021$) (Callens et al., 1998). Anyway, it strongly resembles that signal described in carbonaceous samples as carbon microbeads (Alcántara et al., 2006), coke (Zhecheva et al., 2002) and lignite coals (Taub et al., 2018). It is consistent with the presence of localized radicals in the sample, whose origin has been associated with aromatic π-radicals produced during thermal pyrolisis (Zhecheva et al., 2002), defects in the carbon structure such as dangling bonds with unpaired electrons in the borders of small-size graphene sheets (Alcántara et al., 2006), or carbon-centered radicals with an adjacent oxygen atom (Taub et al., 2018; Green et al., 2014; Menachem el al., 1998).

The radical signal has been detected in archaeological samples even at high temperatures (Robins et al., 1984; Fattibene et al., 2010). In fact, variations of the line width and *g*-values with temperature from 2.0065 (RT) to 2.0035 (500 ºC) for this signal have been reported in carbonized lentil samples, with maximum intensity (and minimum line width in the studied range) around 450 ºC (Aydaş et al., 2010). Other studies reproduce the same trends in the position and line width of the signal with temperature (Bachmann et al., 2007; Rudko et al., 2010). Despite caution must be taken in the comparison with other results and use of these parameters to propose temperatures for thermal processes, the values obtained in the present work would suggest for our carbonized N1 and N2 samples heating temperatures in the 250−450 ºC range.

5. CONCLUSIONS

All the measured samples contain hydroxyapatite partially substituted by carbonate anions, mainly of type B. Calcined B1 and B2, together with the Medieval unburned bones, exhibit the highest crystallinity and lowest carbonate content. The results suggest that B1 and B2 have been heated at temperatures in the 700−800 ºC range, while N1 and N2 at temperatures below 500 ºC.

All the bone samples studied exhibit two kind of EPR signals at $g \approx 2$, a very broad and a radical one, which are not present in the unburned Medieval F1 bone nor in the synthetic hydroxyapatite. The spectra are more intense in the calcined ones, which reveals changes in the magnetic properties of the iron centres (broad band) for the calcined samples B1 and B2. The variation of the energy and line width of the radical signal, together with the colour and IR data, points to temperatures in the 300−450 ºC for the N1 and N2 samples. The same EPR parameters of the radical signal suggest greater annealing temperatures for B1 and B2. The combination of both techniques, the IR and EPR spectroscopies, allows to propose if high crystalline bones, as F1, B1 and B2, have undergone thermal treatment or not.

The results from the multianalytical study of bones from Burial 815, in the Late Pre-Pottery Neolithic B level of Kharaysin site, indicates that they have been cremated. The burned character of the analysed bones confirms the earliest presence of cremated human bones in a funerary context of the Pre-Pottery Neolithic of the Near East in Kharaysin. These cremations constitute an important change in the funeral practices of

686 the Pre-Pottery Neolithic of the Levant. The Kharaysin cremations fit well with the
687 appearance of variations in funerary practices in the central and southern area of the
688 Levant during the Late PPNB (Bocquentin et al., 2016; Ibáñez et al. 2018; Verhoeven
689 2002), that point to initial funerary rite changes that later led to more usual and
690 widespread cremations during the Late Neolithic (Pottery Neolithic) (Croucher 2012;
691 Merpert and Munchaev 1993).

692

693 **6. ACKNOWLEDGMENTS**

694 The authors acknowledge the Consejería de Educación de Castilla y León and FEDER
695 BU291P18, BU022G18 and Ministerio de Economía y Competitividad projects: "Los
696 orígenes del Neolítico en Próximo Oriente: Cambios Ambientales, Económicos, Sociales
697 e Ideológicos (NEOPROX) (HAR2016-74999-P)", CTQ2016-75023-C2-1-P and
698 CTQ2015-70371-REDT MetDrugs Network (Spain) for financing different aspects of
699 this work. Two anonymous reviewers are acknowledged for their constructive and helpful
700 comments that improved the manuscript.

701

702 **7. REFERENCES**

703 Alcántara, R., Ortiz, G.F., Lavela, P., Tirado, J.L., Stoyanova, R., Zhecheva, E. (2006).
704 EPR, NMR, and Electrochemical Studies of Surface-Modified Carbon Microbeads.
705 Chem. Mater. 18, 2293–2301.

706 Almança Lopes, C.D.C., Oliveira Limirio, P.H.J., Novais, V.R., Dechichi, P. (2018).
707 Fourier Transform Infrared Spectroscopy (FTIR) Application Chemical Characterization
708 of Enamel, Dentin and Bone. Appl. Spectrosc. Rev. 53, 747–769.

709 Antonakos, A., Liarokapis, E., Leventouri, T. (2007). Micro-Raman and FTIR studies of
710 synthetic and natural apatites. Biomaterials 28, 3043-3054.

711 Aydaş, C., Engin, B., Dönmez, E.O., Belli, O. (2010). The use of ESR technique for
712 assessment of heating temperatures of archaeological lentil samples. Spectrochim. Acta
713 A 75, 466-473.

714 Bachmann, L., Baffa, O., Zezeli, D.M. (2007). Thermal degradation of dentin collagen
715 evaluated with ESR, infrared and optical spectroscopy. Philos.Mag. 87, 1033-1042.

716 Bertolino, L.C., Malta Rossi, A., Bernstein Scorzelli, R., Lenardo Torem, M. (2010).
717 Influence of iron on kaolin whiteness: an electron paramagnetic resonance study. Appl.
718 Clay Sci. 49, 170-175.

719 Bocquentin, F., Khalaly, H., Bar-Yosef, D., Berna, F., Biton, R., Boness, D., Dubreil, L.,
720 Emery-Barbier, A., Greenberg, H., Goren, Y., Kolska Horwitz, L., Le Dosseur, G.,
721 Lernau, O., Mienis, H.K., Valentin, B., Samuelian, N. (2014). Renewed excavations at
722 Beisamoun: investigating the 7th millennium cal. BC of the southern Levant. J. Israel
723 Prehist. Soc. 44, 5-100.

724 Bocquentin F, Kodas E, and Ortiz A. (2016). Headless but still eloquent! Acephalous
725 skeletons as witnesses of Pre-Pottery Neolithic North-South Levant connections and
726 disconnections. Paléorient 42, 33-52.

727 Bruzek J. 2002. A method for visual determination of sex, using the human hip bone.
728 American Journal of Physical Anthropology 117(2):157-168.

729 Buikstra, J.E. and Swegle, M. (1989). Bone modification due to burning: experimental
730 evidence. In: J.E. Buikstra, M. Swegle, Robson Bonnichsen, H. Sorg. (Eds.). *Bone*
731 *modification*. Orono, ME: Center for the Study of the First Americans, Institute of
732 Quaternary Studies, University of Maine. pp. 247-258.

733 Buikstra, J.E., and Ubelaker, D.H. (1994). Standards for data collection from human
734 skeletal remains: proceedings of a seminar at the Field Museum of Natural History.

735 Butler, D.H., Dawson, P.C. (2013). Accessing hunter-gatherer site structures using
736 Fourier transform infrared spectroscopy: applications at a Taltheilei settlement in the
737 Canadian Sub-Arctic. J. Archaeol. Sci. 40, 731–1742.

738 Callens, F., Vanhaelewyn, G., Matthys, P., Boesman, E. (1998). EPR of carbonate
739 derived radicals: Applications in dosimetry, dating and detection of irradiated food. Appl.
740 Magn. Reson. 14, 235-254.
741 Cardoso, H.F.V. (2008). Age estimation of adolescent and young adult male and female
742 skeletons II, epiphyseal union at the upper limb and scapular girdle in a modern
743 Portuguese skeletal sample. American Journal of Physical Anthropology 137(1):97-105.

744 Cardoso, H.F.V. (2008b). Epiphyseal union at the innominate and lower limb in a modern
745 Portuguese skeletal sample, and age estimation in adolescent and young adult male and
746 female skeletons. .Am. J. Phys. Anthropol., 135(2):161-170.

747 Carrancho, A., Herrejón Lagunilla, A., Vergés, J.M. (2016). Three archaeomagnetic
748 applications of archaeological interest to the study of burnt anthropogenic cave
749 sediments. Quat. Int. 414, 244–257.

750 Cerezo-Román, J.I., Wessman, A., Williams, H. (2017). *Cremation and the Archaeology*
751 *of Death*. Oxford University Press, 364 pp.

752 Coqueugniot H, and Weaver TD. 2007. Brief communication: Infracranial maturation in
753 the skeletal collection from Coimbra, Portugal: New aging standards for epiphyseal
754 union. Am. J. Phys. Anthropol., 134(3):424-437.

755 Croucher, K. (2012). Death and dying in the Neolithic Near East: Oxford University
756 Press, 372 pp.

757 Dal Sasso, G., Lebon, M., Angelini, I., Maritan, L., Usai, D., Artioli, G. (2016). Bone
758 Diagenesis Variability among Multiple Burial Phases at Al Khiday (Sudan) Investigated
759 by ATR-FTIR Spectroscopy. Palaeogeogr. Palaeoclimatol. Palaeoecol. 463, 168–179.

760 de Becdelievre, C., Thiol, S., Santos, F., Rottier, S. (2015). From fire-induced alterations
761 on human bones to the original circumstances of the fire: An integrated approach of
762 human cremains drawn from a Neolithic collective burial. J. Archaeol. Sci. Rep. 4, 210-
763 225.

764 De Leeuw, N. H. (2001). Local ordering of hydroxy groups in hydroxyapatite. Chem.
765 Commun. 1646–1647.

766 Dennison, K.J. and B.M. Peake (1992). ESR bone dating in New Zealand. *Proceedings*
767 *of the 6th International Specialist Seminar on Thermoluminescence and Electron Spin*
768 *Resonance Dating*. Clermond-Ferrand, France. 2–6 July, 1990. Quaternay Sci. Rev.11,
769 251–255.

770 Depierre, G. (2014). *Crémation et archéologie ; Nouvelles alternatives méthodologiques*
771 *en ostéologie humaines*, Éditions Universitaires de Dijon, Collection Art, Archéologie et
772 Patrimoine, Dijon, 654 p.

773 Devlin, J.B. and Herrmann, N.P. (2008). Bone color as an interpretive tool of the
774 depositional history of archaeological cremains. In: Christopher W. Schmidt & Steven A.
775 Symes (Eds.). *The analysis of burned human remains*. Elsevier, pp. 109-128.

776 Diallo-Garcia, S., Ben Osman, M., Krafft, J. M., Boujday, S., Guylène, C. (2014).
777 Discrimination of Infrared Fingerprints of Bulk and Surface POH and OH of
778 Hydroxyapatites. Catal. Today 226, 81–88.

779 Drouet, C., Aufray, M., Rollin-Martinet, S., Vandecandelaère, N., Grossin, D.,
780 Rossignol, F., Champion, E., Navrotsky, A., Rey, C. (2018). Nanocrystalline Apatites:
781 The Fundamental Role of Water. Am. Mineral. 103, 550–564.

782 Edwards, H. G., Villar, S. E. J., Jehlicka, J., & Munshi, T. (2005). FT–Raman
783 spectroscopic study of calcium-rich and magnesium-rich carbonate minerals.
784 Spectrochim. Acta Part A Mol. and Biomol. Spectrosc. 61, 2273-2280.

785 Ellingham, S.T.D., Thompson, T.J.U., Islam, M., Taylor, G. (2015). Estimating
786 Temperature Exposure of Burnt Bone - A Methodological Review. Sci. Justice 55, 181–
787 188.

788 Etok, S.E., Valsami-Jones, E., Wess, T.J., Hiller, J.C., Maxwell, C.A., Rogers, K.D., et
789 al. (2007). Structural and chemical changes of thermally treated bone apatite. J. Mater.
790 Sci. 42, 9807–9816.

791 Fattibene, P., Callens, F. (2010). EPR dosimetry with tool enamel: A review. Appl.
792 Radiat. Isot. 68, 2033-2116.

793 Ferrari, A. C., & Robertson, J. (2000). Interpretation of Raman spectra of disordered and
794 amorphous carbon. Phys. Rev. B 61, 14095-14107.

795 Figueiredo, M., Fernando, A., Martins, G., Freitas, J., Judas, F., Figueiredo, H. (2010).
796 Effect of the calcination temperature on the composition and microstructure of
797 hydroxyapatite derived from human and animal bone. Ceram. Int. 36, 2383–2393.

798 Fleet, M.E. (2009). Infrared Spectra of Carbonate Apatites: N2-Region Bands.
799 Biomaterials 30, 1473–1481.

800 Garstang, J. (1953). *Prehistoric Mersin, Yümük Tepe in southern Turkey*. Oxford:
801 Clarendon Press, 338 pp.

802 Goldstein, L. and Meyers, K. (2014). Transformation and metaphors. Thoughts on
803 cremation practices in the precontact midwestern United States. In: I. Kuijt, C.P. Quinn,
804 G. Cooney (Eds.): *Transformation by Fire, The Archaeology of Cremation in Cultural*
805 *Context*. University of Arizona Press Tucson, Arizona, 352 pp.

806 Gonçalves, D., Thompson, T.J.U & Cunha, E. (2011). Implications of heat-induced
807 changes in bone on the interpretation of funerary behavior and practice. J. Archaeol. Sci.
808 38, 1308-1311.

809 Gonçalves, D. and Pires, A.E. (2017). Cremation under fire: a review of bioarchaeological
810 approaches from 1995 to 2015. Archaeol. Anthropol. Sci. 9, 1677-1688.

811 Gonçalves, D., Vassalo, A.R., Mamede, A.P., Makhoul, C., Piga, G., Cunha, E.,
812 Marques, M.P.M., Batista de Carvalho, L.A.E. (2018). Crystal Clear: Vibrational
813 Spectroscopy Reveals Intrabone, Intraskeleton, and Interskeleton Variation in Human
814 Bones. Am. J. Phys. Anthropol. 166, 296–312.

815 Green, U., Keinan-Adamsky, K., Attia, S., Aizenshtat, Z., Goobes, G., Ruthstein, S.,
816 Cohen, H. (2014). Elucidating the Role of Stable Carbon Radicals in the Low
817 Temperature Oxidation of Coals by Coupled EPR-NMR Spectroscopy-a Method to
818 Characterize Surfaces of Porous Carbon Materials. *Phys. Chem. Chem. Phys.*, 16, 9364–
819 9370.

820 Greiner, M., Rodríguez-Navarro, A., Heiniga, M.F., Mayer, K. Kocsis, B., Göhring, A.,
821 Toncala, A., Grupe, G., Schmahl, W.W. (2019). Bone incineration: An experimental
822 study on mineral structure, colour and crystalline state. J. Archcaeol. Sci. Rep. 25, 507-
823 518.

824 Hayek, E.; Bewesely, H. (1963). Pentacalcium monohydroxyorthophosphate
825 (hydroxyapatite). Inorg. Synth. 7, 63–65.

826 Hummel, S., Schutkowski, H., Herrmann, B. (1988). Advances in cremation research.
827 Actes des 3èmes Journées Anthropologiques 24, 177–194.

828 Ibáñez, J.J., Muñiz, J., Iriarte, E., Monik, M., Santana, J., Teira, L., Corrada, M., Lagüera,
829 M.A., Lendakova, Z., Regalado, E. and Rosillo, R. (2016). Kharaysin: A PPNA and
830 PPNB Site by the Zarqa River. 2014 and 2015 Field Seasons. Neo-Lithics 2/15, 11-19.

831 Ibáñez, J.J., González-Urquijo, J., Teira-Mayolini, L.C., and Lazuén, T. (2018). The
832 emergence of the Neolithic in the Near East: A protracted and multi-regional model. Quat.
833 Int. 470(B), 226-252.

834 Ikeya, M. (1993). New applications of electron spin resonance. Dating, dosimetry and
835 microscopy. World Scientific Publishing Co. Pte. Ltd. Singapore New Jersey London
836 Hong Kong, 1993. 500 pp.

837 Ionescu, C., Hoeck, V., Gruian, C., Simon, V. (2014). Insights into the EPR
838 characteristics of heated carbonate-rich illitic clay. App. Clay Sci. 97-98, 138-145.

839 Kaleidagraph v4.1.1 Synergy Software, 2010.

840 Kontopoulos, I., Presslee, S., Penkman, K., Collins, M.J. (2018). Vibrational
841 Spectroscopy Preparation of Bone Powder for FTIR-ATR Analysis: The Particle Size
842 Effect. Vib. Spectrosc. 99, 167–177.

843 Kontopoulos, I., Penkman, K., Mcallister, G.D., Lynnerup, N., Damgaard, P.B., Hansen,
844 H.B., Allentoft, M.E., Collins, M.J. (2019). Petrous Bone Diagenesis : A Multi-Analytical
845 Approach. Palaeogeogr. Palaeoclimatol. Palaeoecol. 518, 143–154.

846 Koon, H.E.C., Nicholson, R.A., Collins, M.J. (2003). A Practical Approach to the
847 Identification of Low Temperature Heated Bone Using TEM. J. Archaeol. Sci. 30, 1393–
848 1399.

849 Kostadinova-Avramova, M., Kovacheva, M. (2013). The magnetic properties of baked
850 clays and their implications for past geomagnetic field intensity determinations. Geophys.
851 J. Int. 195, 1534–1550.

852 Larsson, A., Nilsson Stutz, L. (2014). Reconcilable differences: cremation, fragmentation
853 and inhumation in Mesolithic and Neolithic Sweden. In: I. Kuijt, C.P. Quinn, G. Cooney
854 (Eds.): *Transformation by Fire, The Archaeology of Cremation in Cultural Context*.
855 University of Arizona Press Tucson, Arizona, 47-66.

856 Lebon, M., Reiche, I., Fröhlich, F., Bahain, J., Falguères, C. (2008). Characterization of
857 Archaeological Burnt Bones: Contribution of a New Analytical Protocol Based on
858 Derivative FTIR Spectroscopy and Curve Fitting of the ν_1 ν_3 PO_4 Domain. Anal. Bioanal.
859 Chem. 392, 1479–1488.

860 Lee Thorp, J.A., Sponheimer, M. (1999). Alteration of Enamel Carbonate Environments
861 during Fossilization. J. Archaeol. Sci. 26, 143–150.

862 LeGeros, R. Z., Trautz, O.R., Klein, E., LeGeros, J. P. (1969). Problem Should Induce
863 Qualified Experimental Studies To Elucidate the Cocarcinogenic Mechanism At the
864 Molecular Level. Experientia 25, 5–7.

865 Mamede, A.P., Vassalo, A.R., Piga, G., Cunha, E., Parker, S.F., Marques, M.P.M.,
866 Batista De Carvalho, L.A.E., Gonçalves, D. (2018a). Potential of Bioapatite Hydroxyls
867 for Research on Archeological Burned Bone. Anal. Chem. 90, 11556–11563.

868 Mamede, A.P., Gonçalves, D., Marques, M.P.M., Batista de Carvalho, L.A.E. (2018b).
869 Burned Bones Tell Their Own Stories: A Review of Methodological Approaches to
870 Assess Heat-Induced Diagenesis. Appl. Spectrosc. Rev. 53, 603–635.

871 Marques, M.P.M., Gonçalves, D., Amarante, A.I.C., Makhoul, C.I., Parker, S.F., Batista
872 De Carvalho, L.A.E. (2016). Osteometrics in Burned Human Skeletal Remains by
873 Neutron and Optical Vibrational Spectroscopy. RSC Adv. 6, 68638–68641.

874 Marques, M.P.M., Mamede, A.P., Vassalo, A.R., Makhoul, C., Cunha, E., Gonçalves,
875 D., Parker, S.F., Batista de Carvalho, L.A.E. (2018). Heat-Induced Bone Diagenesis
876 Probed by Vibrational Spectroscopy. Sci. Rep. 8, 1–13.

877 Mayne Correia, P.M. (1997). Fire modification of bone: a review of the literature. In:
878 Haglund, W.D., Sorg, M.H. (Eds.), Forensic *Taphonomy : The Postmortem*
879 *Fate of Human Remains*. CRC Press, Boca Raton, FL, 275 –293.

880 Mekhemer, G.A.H., Bongard, H., Shahin, A.A.B., Zaki, M.I. (2019). FTIR and Electron
881 Microscopy Observed Consequences of HCl and CO_2 interfacial Interactions with
882 Synthetic and Biological Apatites: Influence of Hydroxyapatite Maturity. Mater. Chem.
883 Phys. 221, 332–341.

884 Menachem, C., Wang, Y., Flowers, J., Peled, E., Greenbaum, S. G. (1998).
885 Characterization of Lithiated Natural Graphite before and after Mild Oxidation. J. Power
886 Sources 76, 180–185.

887 Menzel, B., Amberg, C. H. (1972). An Infrared Study of the Hydroxyl Groups in a
888 Nonstoichiometric Calcium Hydroxyapatite with and without Fluoridation. J. Colloid
889 Interface Sci. 38, 256–264.

890 Merpert, N.I. and Munchaev, R.M. (1993). *Burial Practices of The Halaf Culture. Early*
891 *Stages in the Evolution of Mesopotamian Civilization: Soviet Excavations in Northern*
892 *Iraq*. University of Arizona Press, Tucson, pp. 207-222.

893 Monge, G., Carretero, M.I., Pozo, M., Barroso, C. (2014). Mineralogical Changes in
894 Fossil Bone from Cueva Del Angel, Spain: Archaeological Implications and Occurrence
895 of Whitlockite. J. Archaeol. Sci. 46, 6–15.

896 Monnier, G. F. (2018). A Review of Infrared Spectroscopy in Microarchaeology:
897 Methods, Applications, and Recent Trends. J. Archaeol. Sci. Reports 18, 806–823.

898 Munro, L.E., Longstaffe, F.J., White, C.D. (2007). Burning and Boiling of Modern Deer
899 Bone: Effects on Crystallinity and Oxygen Isotope Composition of Bioapatite Phosphate.
900 Palaeogeogr. Palaeoclimatol. Palaeoecol. 249, 90–102.

901 Nagy, G., Lorand, T., Patonai, Z., Montsko, G., Bajnoczky, I., Marcsik, A., Mark, L.
902 (2008). Analysis of Pathological and Non-Pathological Human Skeletal Remains by FT-
903 IR Spectroscopy. Forensic Sci. Int. 175, 55–60.

904 Nicholson, R.A. (1993). A Morphological Investigation of Burnt Animal Bone and an
905 Evaluation of its Utility in Archaeology. J. Archaeol. Sci. 20, 411-428.

906 Oduwole, A.D., Sales, K.D., Dennison, K.J. (1993). Some ESR observations on bone,
907 tooth enamel and eggshell. Appl. Radiat. Isot. 44, 1-2, 261-266.

908 Olsen, J., Heinemeier, J., Bennike, P., Krause, C., Margrethe Hornstrup, K., Thrane, H.
909 (2008). Characterisation and Blind Testing of Radiocarbon Dating of Cremated Bone. J.
910 Archaeol. Sci. 35, 791–800.

911 Olsen, J., Heinemeier, J., Hornstrup, K.M., Bennike, P., Thrane, H. (2013). 'Old wood'
912 effect in radiocarbon dating of prehistoric cremated bones? J. Archaeol. Sci. 40, 30–34.

913 Person, A., Bocherens, H., Saliège, J.-F., Paris, F., Zeitoun, V. & Gérard, M. (1995).
914 Early diagenetic evolution of bone phosphate: an X-ray diffractometry analysis. J.
915 Archaeol. Sci. 22, 211-221.

916 Piga, G., Guirguis, M., Bartoloni, P., Malgosa, A., Enzo, S. (2010a). A Funerary Rite
917 Study of the Phoenician-Punic Necropolis of Mount Sirai (Sardinia, Italy). Int. J.
918 Osteoarchaeol. 20, 144–157.

919 Piga G., Hernández-Gasch J.H, Malgosa A., Ganadu M.L, Enzo S. (2010b). Cremation
920 practices coexisting at the S'Illot des Porros Necropolis during the Second Iron Age in
921 the Balearic Islands (Spain). Homo 61, 440–452.

922 Piga, G.; Malgosa, A.; Thompson, T. J. U.; Guirguis, M.; Enzo, S. A (2015). Unique
923 Case of Prone Position in the Primary Cremation Tomb 252 of Monte Sirai Necropolis (
924 Carbonia , Sardinia , Italy). Int. J. Osteoarchaeol. 159, 146–159.

925 Piga, G., Solinas, G., Thompson, T. J. U., Brunetti, A., Malgosa, A., Enzo, S. (2013). Is
926 X-ray diffraction able to distinguish between animal and human bones?. J. Archaeol. Sci.
927 40, 778–785.

928 Piga, G., Guirguis, M., Thompson, T. J. U., Isidro, A., Enzo, S., Malgosa, A. (2016). A
929 case of semi-combusted pregnant female in the Phoenician-Punic necropolis of Monte
930 Sirai (Carbonia, Sardinia, Italy). HOMO-Journal of Comparative Human Biology, 67, 50-
931 64.

932 Piga, G., Malgosa, A., Thompson, T.J.U., Enzo, S. (2008). A new calibration of the XRD
933 technique for the study of archaeological burned human remains. J. Archaeol. Sci. 35,
934 2171-2178.

935 Piga, G., Amarante, A., Makhoul, C., Cunha, E., Malgosa, A., Enzo, S., Gonçalves, D.
936 (2018). β-Tricalcium Phosphate Interferes with the Assessment of Crystallinity in Burned
937 Skeletal Remains. J. Spectrosc. 2018, (Article ID 5954146),
938 https://doi.org/10.1155/2018/ 5954146.

939 Piga, G., Baró, M.D., Escobal, I.G., Gonçalves, D., Makhoul, C., Amarante, A., Malgosa,
940 A., Enzo, S., Garroni, S. (2016a). A Structural Approach in the Study of Bones: Fossil
941 and Burnt Bones at Nanosize Scale. Appl. Phys. A Mater. Sci. Process. 122, 1–12.

942 Piga, G., Gonçalves, D., Thompson, T. J. U., Brunetti, A., Malgosa, A., Enzo, S. (2016b).
943 Understanding the Crystallinity Indices Behavior of Burned Bones and Teeth by ATR-
944 IR and XRD in the Presence of Bioapatite Mixed with Other Phosphate and Carbonate
945 Phases. Int. J. Spectrosc. *2016* (January), Article ID 4810149.

946 Pon-On, W., Meejoo, S., Tang, I.M. (2007). Incorporation of iron into nano
947 hydroxyapatite particles synthesized by the microwave process. Int. Jour. Nanosc. 6, 9-
948 16.

949 Reidsma, F.H., Hoesel, A. Van, Os, B. J. H. Van, Megens, L., Braadbaart, F. (2016).
950 Charred Bone: Physical and Chemical Changes during Laboratory Simulated Heating
951 under Reducing Conditions and Its Relevance for the Study of Fire Use in Arcchaelogy.
952 J. Archaeol. Sci. Rep. 10, 282–292.

953 Rey, C., Collins, B., Goehl, T., Dickson, I. R, Glimcher, M. J. (1989). The Carbonate
954 Environment in Bone Mineral: A Resolution-Enhanced Fourier Transform Infrared
955 Spectroscopy Study. Calcif. Tissue Int. 45, 157–164.

956 Robins, G.V., Sales, K.D., McNeil, D.A.C. (1984). Ancient spins. *Chem. Br.*, 20, 894-
957 899.

958 Rudko, V.V., Vorona, I.P., Baran, N.P., Ishchencko, S.S., Zatovsky, I.V., Chumakova,
959 L.S. (2010). The mechanism of CO_2 radical formation in biological and synthetic apatites.
960 Health Phys. 98, 322-326.

961 Schiegl, S., Goldberg, P., Pfretzschner, H.U., Conard, N.J. (2003). Paleolithic Burnt
962 Bone Horizons from the Swabian Jura: Distinguishing between in Situ Fireplaces and
963 Dumping Areas. Geoarchaeology 18, 541–565.

964 Schmidt, C. and Symes, S. (2015). *The analysis of burned human remains*. 2nd Edition,
965 Academic Press, 448 pp.

966 Schmidt, F.N., Zimmermann, E.A., Campbell, G.M., Sroga, G.E., Püschel, K., Amling,
967 M., Tang, S.Y., Vashishth, D., Busse, B. (2017). Assessment of Collagen Quality
968 Associated with Non-Enzymatic Cross-Links in Human Bone Using Fourier-Transform
969 Infrared Imaging. Bone 97, 243–251.

970 Scorrano, G., Mazzuca, C., Valentini, F., Scano, G., Buccolieri, A., Giancane, G.,
971 Manno, D., Valli, L., Mallegni, F., Serra, A. (2017). The Tale of Henry VII: A
972 Multidisciplinary Approach to Determining the Post-Mortem Practice. Archaeol.
973 Anthropol. Sci. 9, 1215–1222.

974 Shipman, P., Foster, G., Schoeninger, M. (1984). Burnt bones and teeth: an experimental
975 study of color, morphology, crystal structure and shrinkage. J. Archaeol. Sci. 11, 307-
976 325.

977 Snoeck, C., Schulting, R. J. (2014). From Bone to Ash : Compositional and Structural
978 Changes in Burned Modern and Archaeological Bone. Palaeogeogr. Palaeoclimatol.
979 Palaeoecol. 416, 55–68.

980 Sponheimer, M., Lee Thorp, J. A. (1999). Alteration of Enamel Carbonate Environments
981 during Fossilization. J. Archaeol. Sci., 26, 143–150.

982 Squires, K. E., Thompson, T.J.U., Islam, M., Chamberlain, A. (2011). The Application
983 of Histomorphometry and Fourier Transform Infrared Spectroscopy to the Analysis of
984 Early Anglo-Saxon Burned Bone. J. Archaeol. Sci., 38, 2399–2409.

985 Stiner, M.C., Kuhn, S.L., Weiner, S., Bar-Yosef, O. (1995). Differential Burning,
986 Recrystallization, and Fragmentation of Archaeological Bone. J. Archaeol. Sci., 22, 223-
987 237.

988 Stiner, M.C., Kuhn, S.L., Surovell, T.A., Goldberg, P., Meignen, L., Weiner, S., Bar-
989 Yosef, O. (2001). Bone Preservation in Hayonim Cave (Israel): A Macroscopic and
990 Mineralogical Study. J. Archaeol. Sci., 28, 643–659.

991 Subira, M.E., Malgosa, A. (1993). The effect of cremation on the study of trace elements.
992 Int. J. of Osteoarchaeol. 3, 115-118.

993 Surovell, T.A., Stiner, M.C. (2001). Standardizing Infra-Red Measures of Bone Mineral
994 Crystallinity: An Experimental Approach. J. Archaeol. Sci. 28, 633–642.

995 Symes, S.A. (1996). Bones: bullets, burns, bludgeons, blunders, and why (Workshop).
996 Proceedings of the American Academy of Forensic Sciences 2, 10-11.

997 Taub, T., Ruthstein, S., Cohen, H. (2018). The Involvement of Carbon-Centered Radicals
998 in the Aging Process of Coals under Atmospheric Conditions: An EPR Study. Phys.
999 Chem. Chem. Phys. 20, 27025–27035.

1000 Tema, E., Ferrara, E. (2019). Magnetic measurements as indicator of the equivalent firing
1001 temperature of ancient baked clays: new results, limits and cautions. J. Cult. Herit. 35,
1002 64–75.

1003 Thompson, T.J.U., Islam, M., Piduru, K., Marcel, A. (2011). An Investigation into the
1004 Internal and External Variables Acting on Crystallinity Index Using Fourier Transform
1005 Infrared Spectroscopy on Unaltered and Burned Bone. Palaeogeogr. Palaeoclimatol.
1006 Palaeoecol. 299, 168–174.

1007 Thompson, T.J.U., Islam, M., Bonniere, M. (2013). A New Statistical Approach for
1008 Determining the Crystallinity of Heat-Altered Bone Mineral from FTIR Spectra. J.
1009 Archaeol. Sci., 40, 416–422.

1010 Thompson, T.J.U. (ed.) (2015a). The archaeology of cremation: burned human remains
1011 in funerary studies: Oxbow Books, 256 pp.

1012 Thompson, T. J. U. (2015b). The analysis of heat-induced crystallinity change in bone.
1013 In: Schmidt, C. W., Symes, S. A. (Eds.). *The analysis of burned human remains*. 2nd Ed.,
1014 Academic Press, 2015.

1015 Thompson, T.J.U., Gauthier, M., Islam, M. (2009). The Application of a New Method of
1016 Fourier Transform Infrared Spectroscopy to the Analysis of Burned Bone. J. Archaeol.
1017 Sci. 36, 910–914.

1018 Tsuneki, A. (2011). A glimpse of human life from Neolithic cemetery at Tell el-Kerkh,
1019 Northwest Syria. Documenta Praehistorica, XXXVIII, 83-95.

1020 Uberlaker, D., Scammell, H. (1992). *Bones: A forensic detective's case book.* New York:
1021 Harper Collins. 1992. xiii + 317 pp.

1022 Verhoeven M. (2002). Transformations of Society: The Changing Role of Ritual and
1023 Symbolism in the PPNB and the PN in the Levant, Syria and South-East Anatolia.
1024 Paleorient 28, 5-13.

1025 Walker, M.J., Angelucci, D.E., Avilés-Fernández, A., Berna, F., Buitrago-López, A.T.,
1026 Fernández-Jalvo, J., Haber-Uriarte, M., López-Jiménez, A., López-Martínez, M., Martín-
1027 Lerma, I., et al. (2016). Findings , context , and significance of combustion at the Late
1028 Early Pleistocene Palaeolithic site of Cueva Negra del Estrecho del Rio. Antiquity 90,
1029 571–589.

1030 Walker, P.L., Miller, K.W., Richman, R. (2008). Time, Temperature, and Oxygen
1031 Availability-7: An Experimental Study of the Effects of Environmental Conditions on the
1032 Color and Organic Content of Cremated Bone. *In*: Schmidt, C. & Symes, S. (Eds.). *The*
1033 *Analysis of Burned Human Remains*. 1st Edition, Academic Press, San Diego, 296 pp.

1034 Wang, X.Y., Zuo, Y., Huang, D., Hou, X.D., Li, Y.B. (2010). Comparative study on
1035 inorganic composition and crystallographic properties of cortical and cancellous bone.
1036 Biomed. Environ. Sci. 23, 473–480.

1037 Weiner, S., Bar-Yosef, O. (1990). States of preservation of bones from prehistoric sites
1038 in the Near East: a survey. J. Archaeol. Sci. 17, 143–150.

1039 WINEPR SimFonia v1.25, Bruker Analytische Messtecnik GmßH, 1996.

1040 Wopenka, B., & Pasteris, J. D. (2005). A mineralogical perspective on the apatite in bone.
1041 *Materials Science and Engineering*: C 25, 131-143.

1042 Zhecheva, E., Stoyanova, R., Jiménez-Mateos, J. M., Alcántara, R., Lavela, P., Tirado,
1043 J. L. (2002). EPR Study on Petroleum Cokes Annealed at Different Temperatures and
1044 Used in Lithium and Sodium Batteries. Carbon N. Y. 40, 2301–2306.

1045

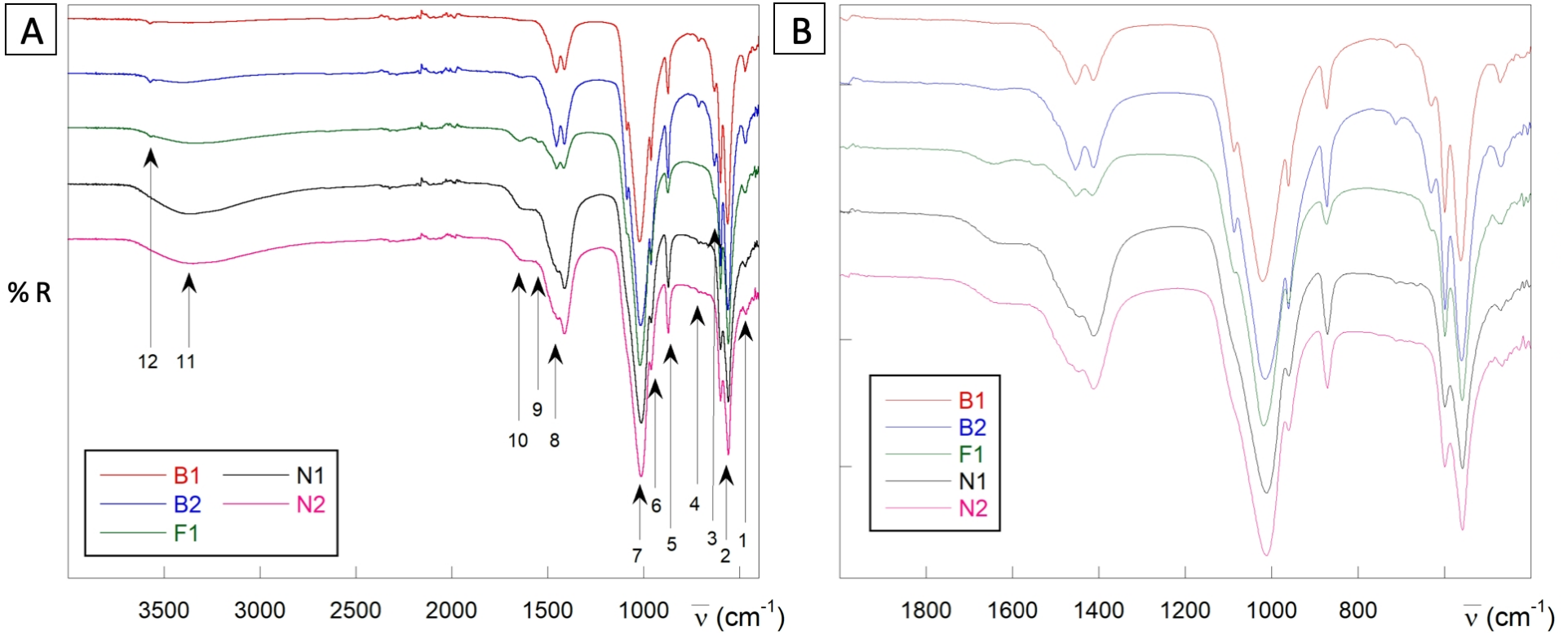
A
% R
12
11
10
9
8
7
6
5
4
3
2
1
B1
B2
F1
N1
N2
3500
3000
2500
2000
1500
1000
ν (cm-1)
B
1800
1600
1400
1200
1000
800
ν (cm-1)

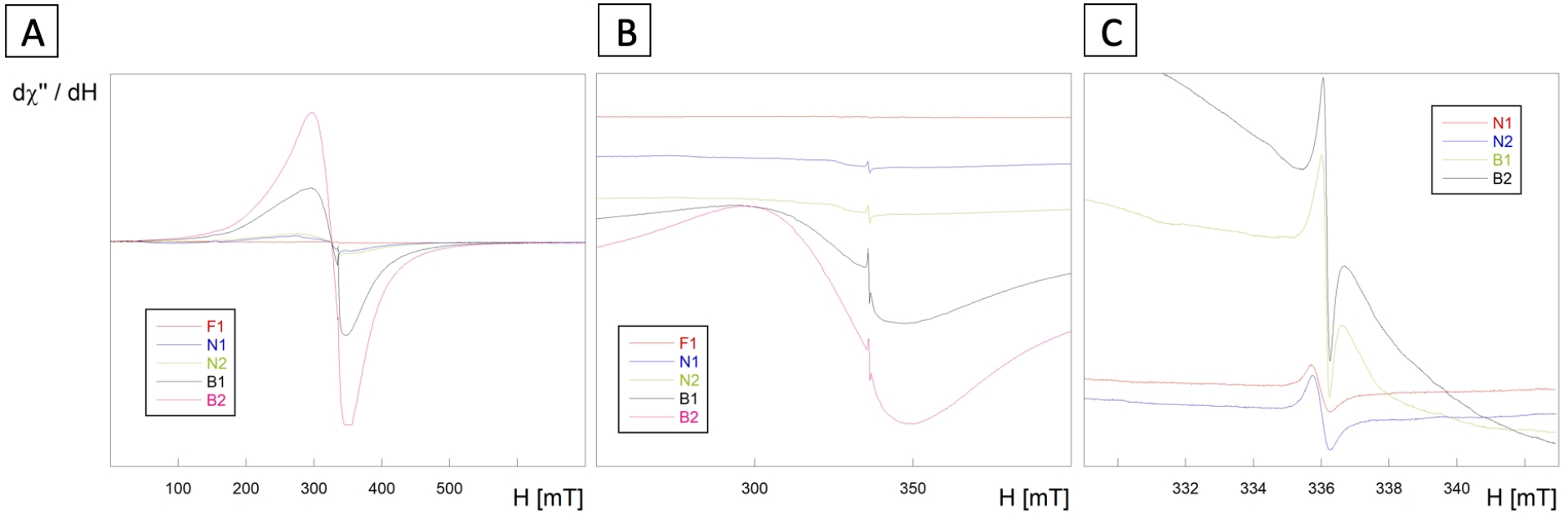
A
B
C
dχ" / dH
F1
N1
N2
B1
B2
100
200
300
400
500
H [mT]
300
350
H [mT]
N1
N2
B1
B2
332
334
336
338
340
H [mT]

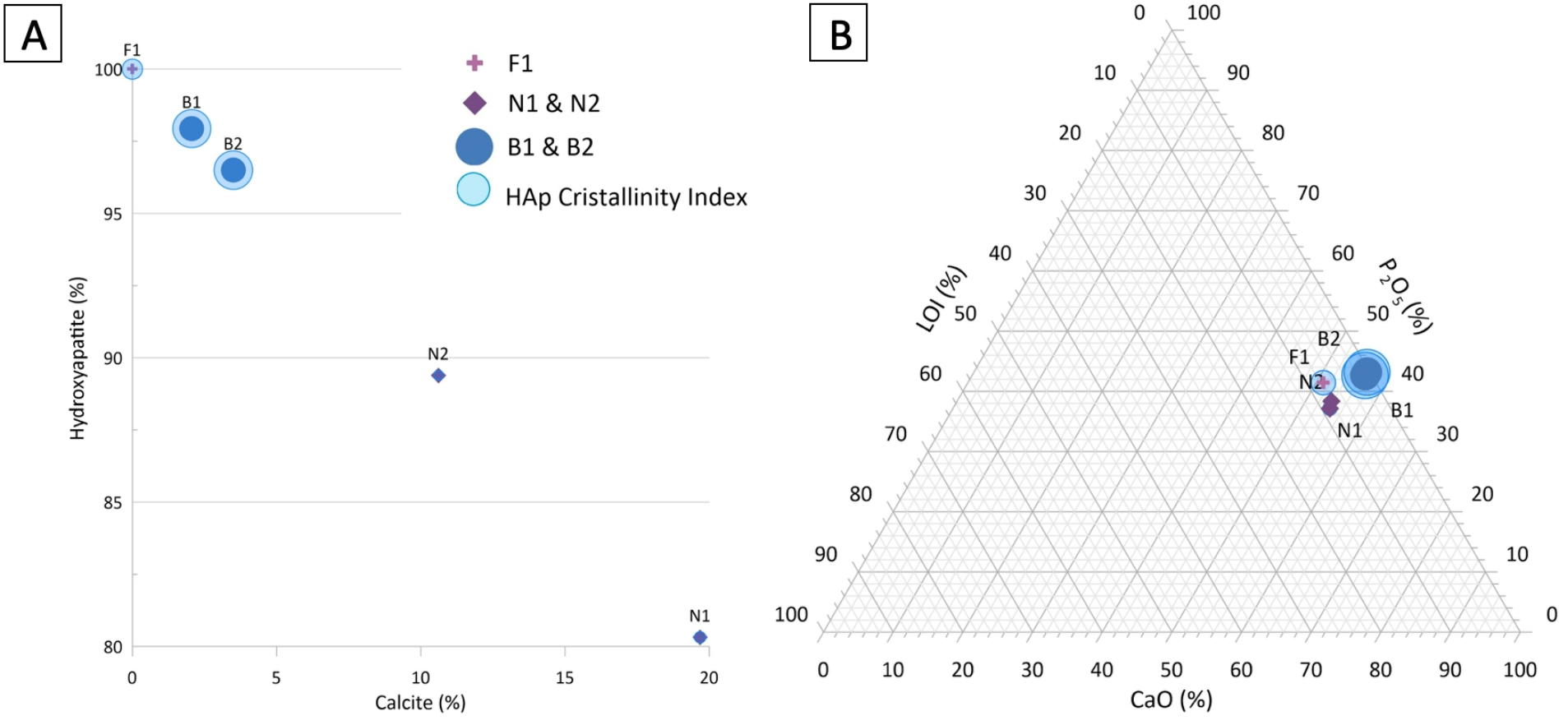
A
F1
B1
B2
N2
N1
100
95
90
85
80
0
5
10
15
20
Hydroxyapatite (%)
Calcite (%)
F1
N1 & N2
B1 & B2
HAp Cristallinity Index
B
LOI (%)
P2O5 (%)
CaO (%)
F1
N2
B2
B1
N1

Declaration of interests

 The authors declare that they have no known competing financial interests or personal relationships that could have appeared to influence the work reported in this paper.

☐The authors declare the following financial interests/personal relationships which may be considered as potential competing interests:

Geochemical and spectroscopic approach to the characterization of earliest cremated human bones from the Levant (PPNB of Kharaysin, Jordan)

by

Iriarte, E., García-Tojal, J., Santana, J., Jorge, S., Teira, L., Muñiz, J., Ibañez, J.J.

SUPPLEMENTARY INFORMATION

7.1. Radiocarbon dating

Different approaches were applied to directly date the bone remains from the burial. Standard radiaocarbon dating was not successful due to the lack of organic material in bones. We therefore selected totally cremated chalky-white bone samples to date them after bone carbonate extraction (acid wash prior to acidification). When bones are heated above 600°C, the osteocalcin (bioapatite) in the bone is converted to structural carbonate. This bone carbonate could be dated. The structural carbonate is very resistant to change and not easily contaminated once cremation has occurred, therefore it has been shown to be a good substance for reliable AMS dating. This second approach was successful and one dating was obtained. Datings were performed using AMS method in Beta Analytic Laboratories and were calibrated using Oxcal software and Intcal´13 calibration curve (Ramsey, 2009; Reimer et.al., 2013).

The radiocarbon dating of a chalky-white sample from the 815 Burial in Kharaysin site yielded and age of 8010 ± 30 BP, corresponding to 9007-8774 yr cal BP (7058-6825 cal BC). This age is in good agreement with the archaeological remains and context of the burial suggesting a Late PPNB age.

7.2. Synthetic hydroxyapatite preparation (Hayek et al., 1963)

Concentrated HNO_3 was dropwise added over solid $CaCO_3$ (3.00 g, 30 mmol) with continuous stirring inside a hood. Once dissolved, 20 ml of distilled water were poured over the solution and, afterwards, a freshly prepared NaOH 10 M aqueous solution was carefully added with stirring just to reach pH 12, with a strict control of pH to avoid exceeding this pH value because it would provoke the precipitation of $Ca(OH)_2$. This solution was filtered off. Another aqueous solution was prepared dissolving $(NH_4)_2HPO_4$ (2.64 g, 20 mmol) in 50 ml of water, followed by addition of NaOH 10 M to reach pH

12. The last solution was filtered off, transfered to a dropping funnel and very slowly added over the boiling Ca(II) solution with stirring. Once the addition was finished, the solution was kept with stirring and boiling for 10 min. The white precipitate was filtered off and washed with boiling water (150 ml) and acetone (30 ml), dried in a stove at 240 ºC for 2 h and, finally, heated in an owen at 800 ºC overnight. The compound was characterised by X-ray powder diffraction and infrared spectroscopy.

7.3. DRX, XRF and LOI analyses

Figure S1. XRD diffractograms of analysed bone samples.

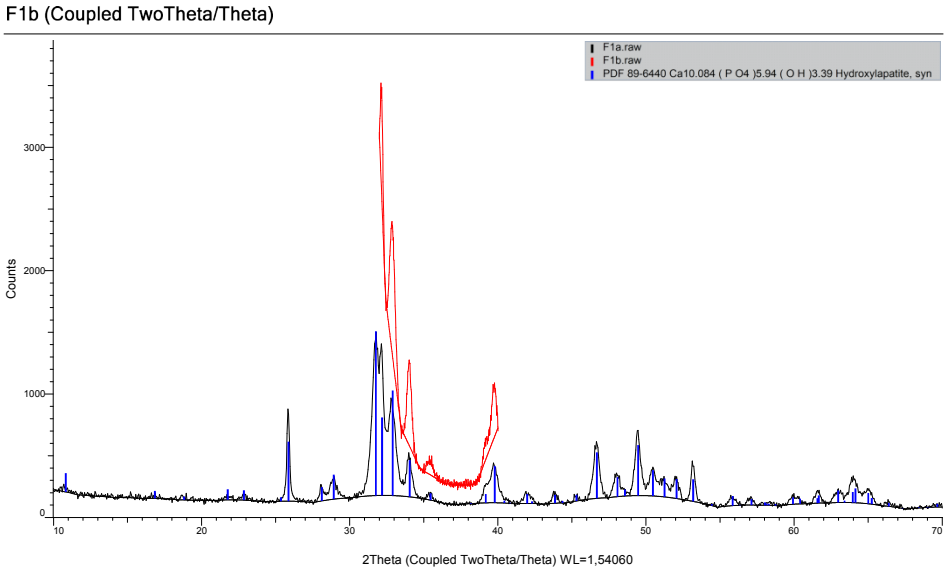

N1b (Coupled TwoTheta/Theta)

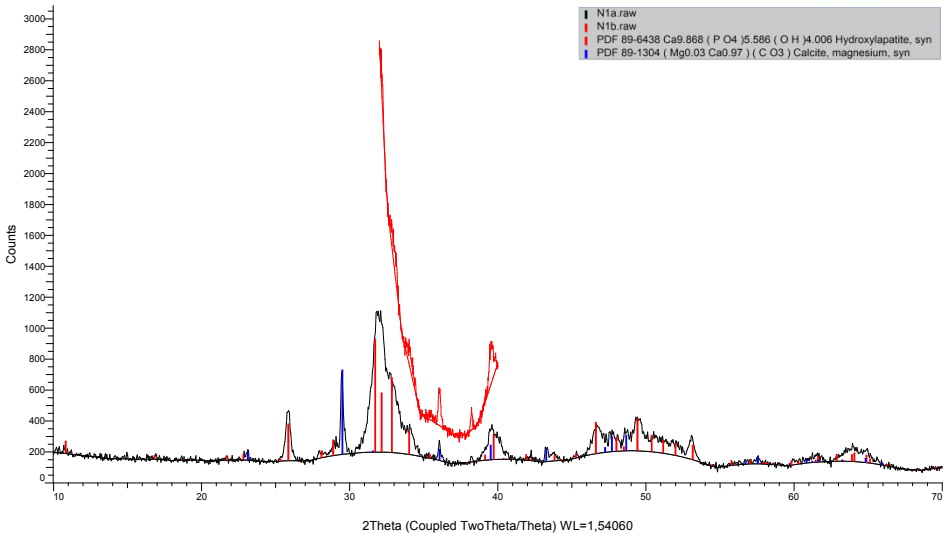

N2b (Coupled TwoTheta/Theta)

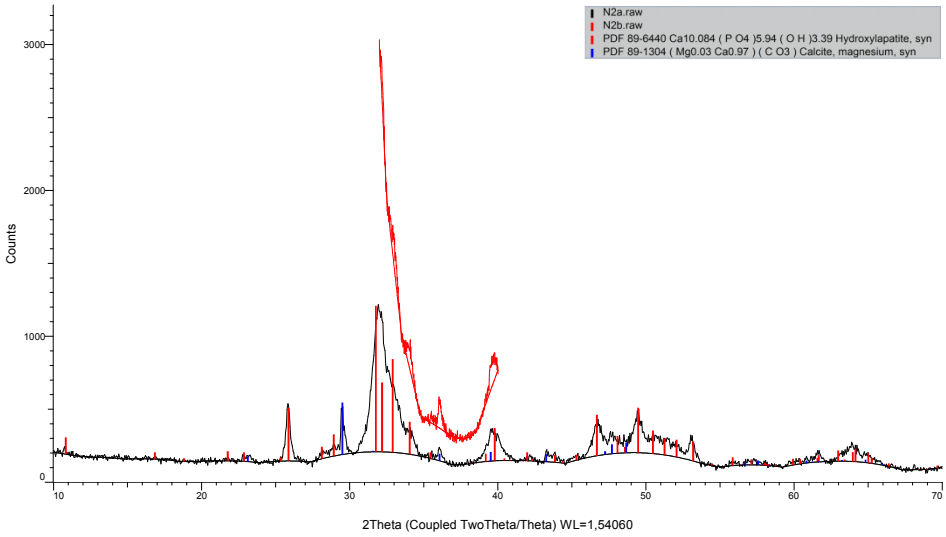

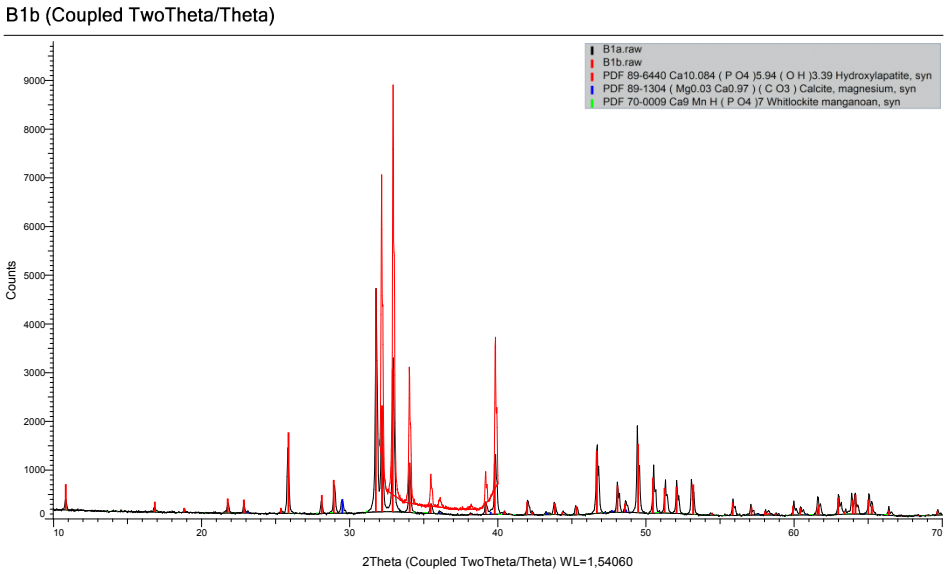

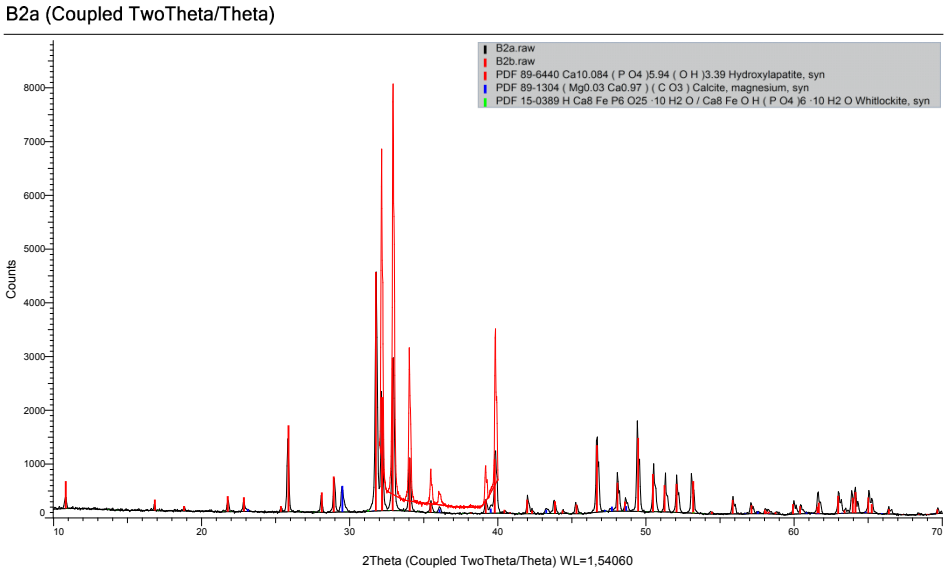

7.4. FTIR Analysis

Figure S2. (a) Infrared spectra of synthetic hydroxyapatite. (b) Magnification of the 2000-4000 cm^{-1} region.

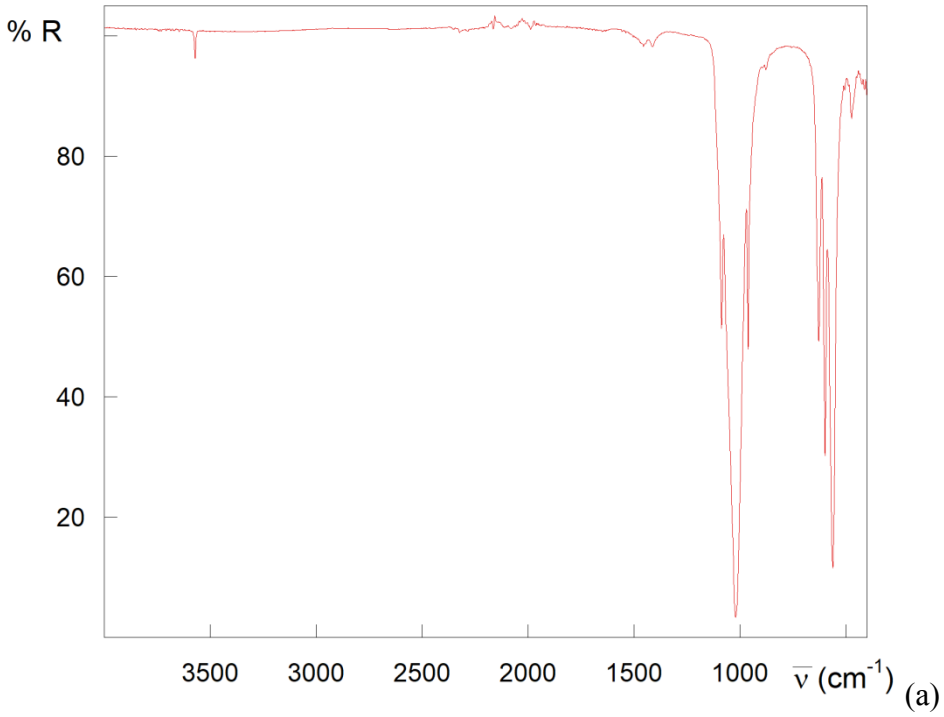

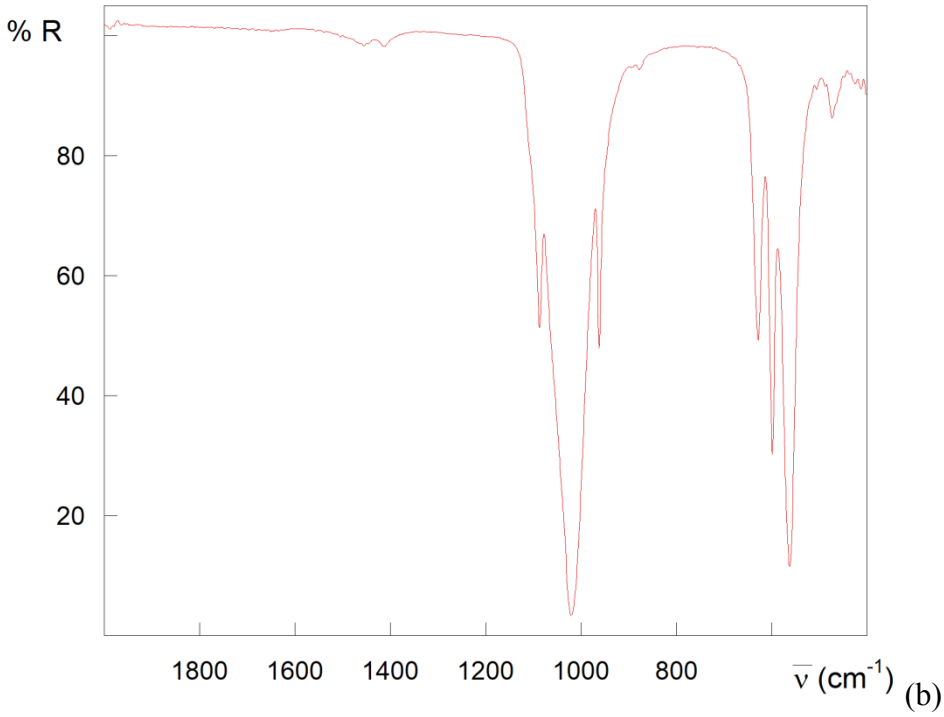

Figure S3. (a) Infrared spectra of calcined bone samples (B1 in red, B2 blue). (b) Magnification of the 2000-4000 cm^{-1} region.

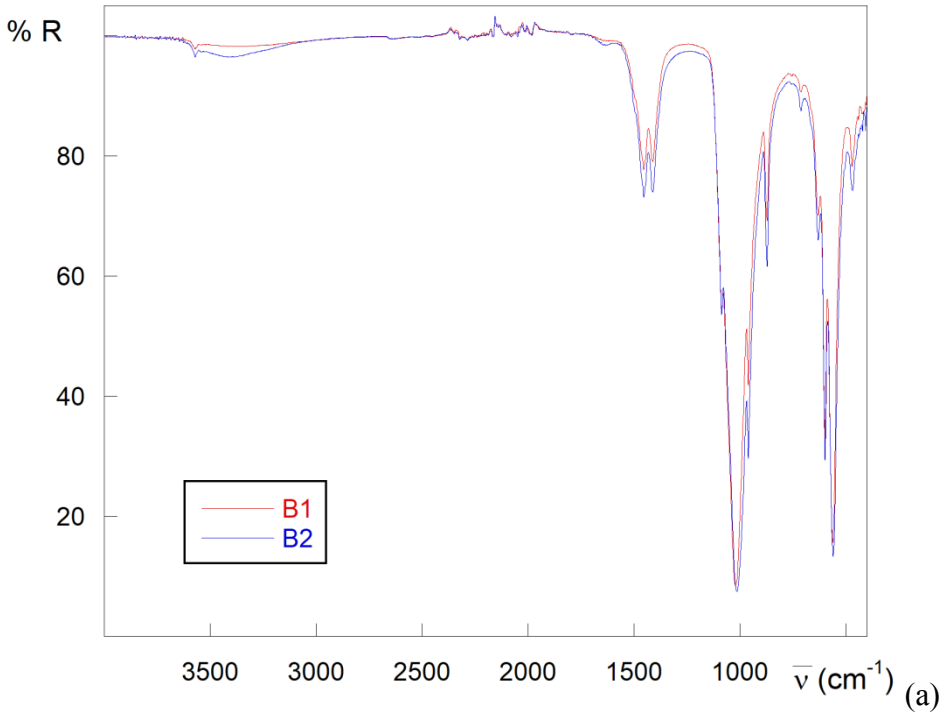

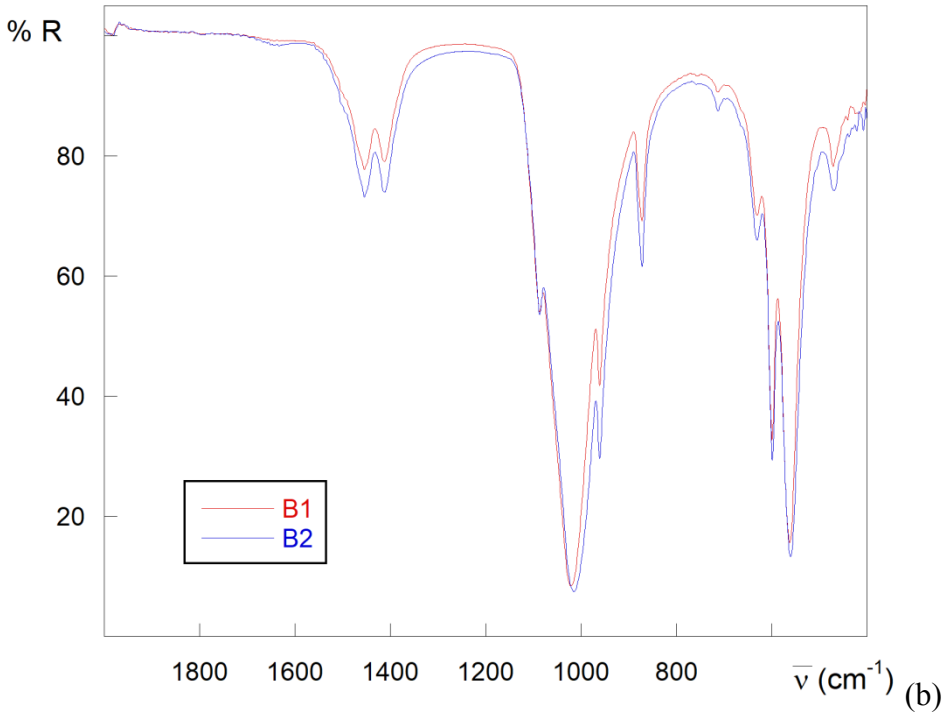

Figure S4. (a) Comparison between the infrared spectra of the calcined bone sample B1 and hydroxyapatite synthesised at 800 ºC. (b) Magnification of the 2000-4000 cm^{-1} region.

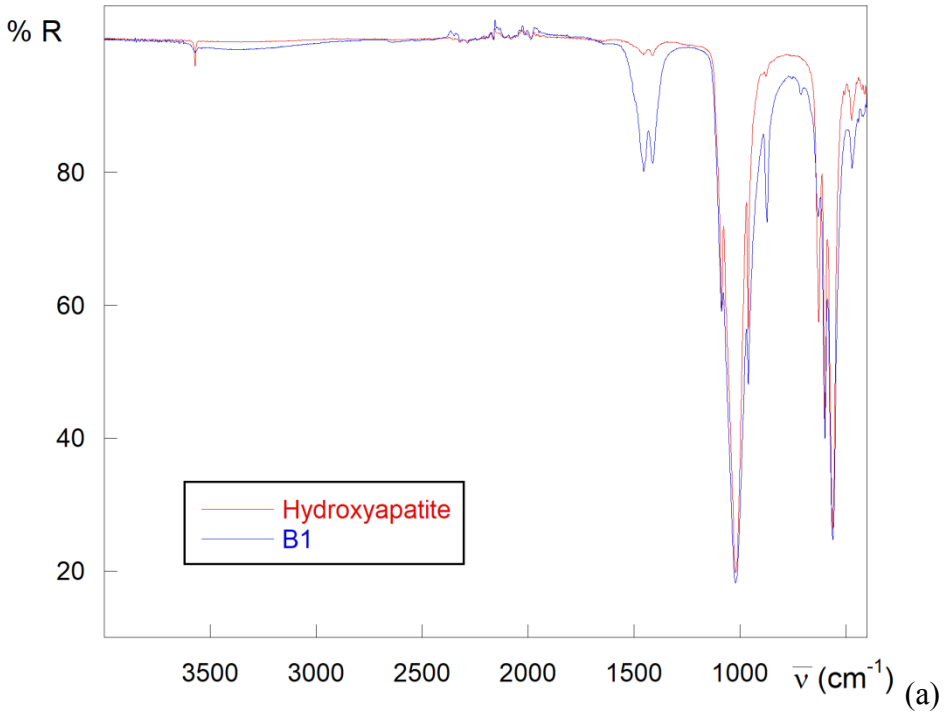

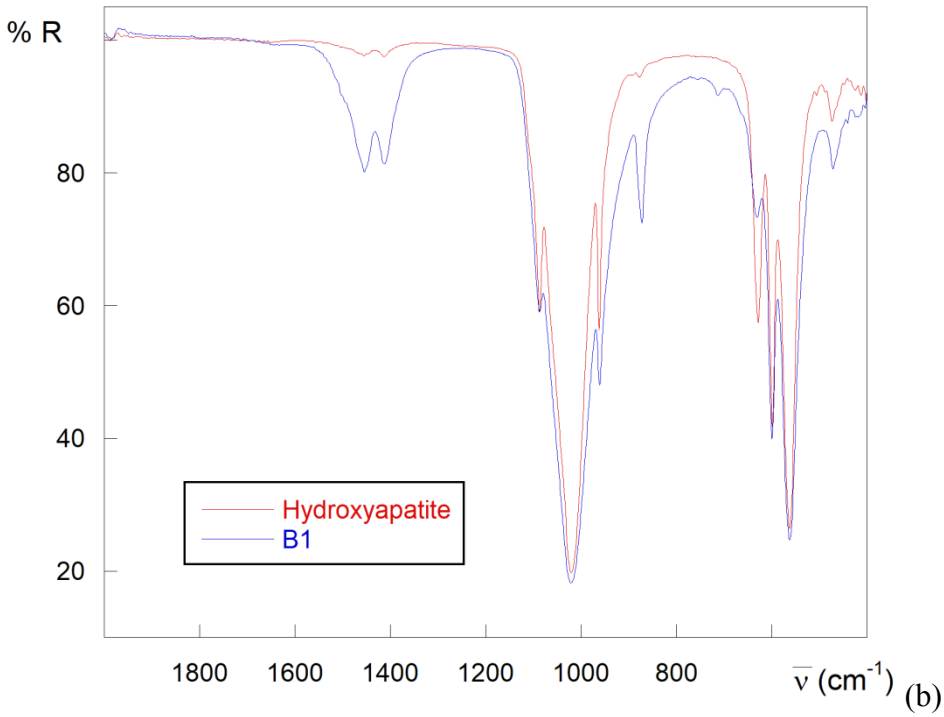

Figure S5. Magnification of the infrared bands attributed to $\nu_2(CO32-)$ modes for calcined bone samples (B1 red, B2 blue), a Middle Ages bone sample (F1, green), and dark carbonized bone samples (N1 black, N2 pink).

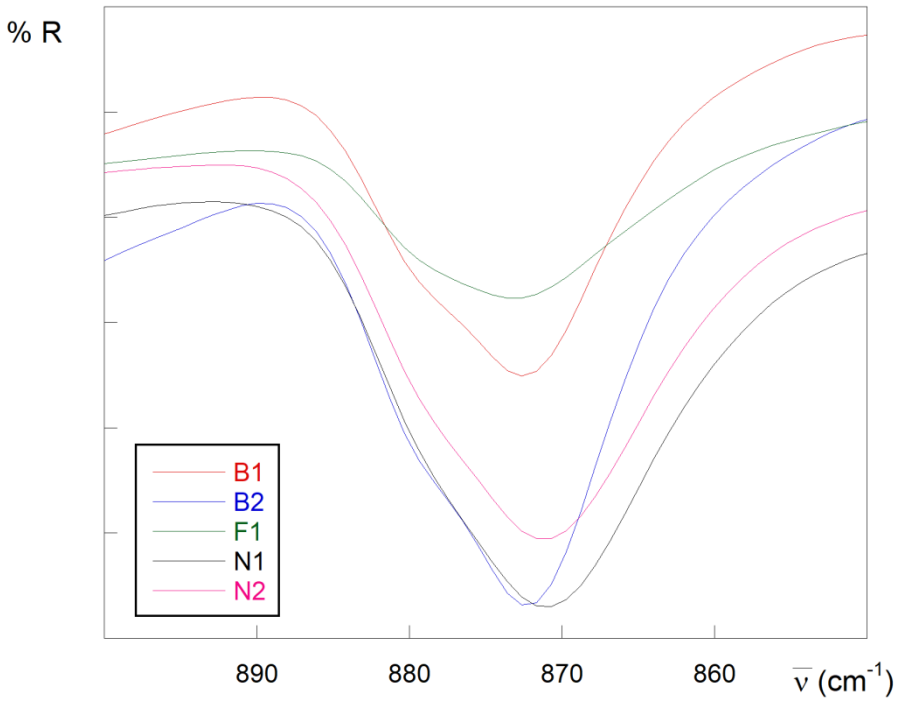

Figure S6. Details of calculations of values of the indices of Table IV for the case of F1. (a) 750–450 cm^{-1} region, the base line correction has been performed fitting to zero the absorbance at 750 and 450 cm^{-1}. (b) 895–835 cm^{-1} region, the base line correction has been performed fitting to zero the absorbance at 895 and 835 cm^{-1}. (b) 1590–1300 cm^{-1} region, the base line correction has been performed fitting to zero the absorbance at 1590 and 1300 cm^{-1}.

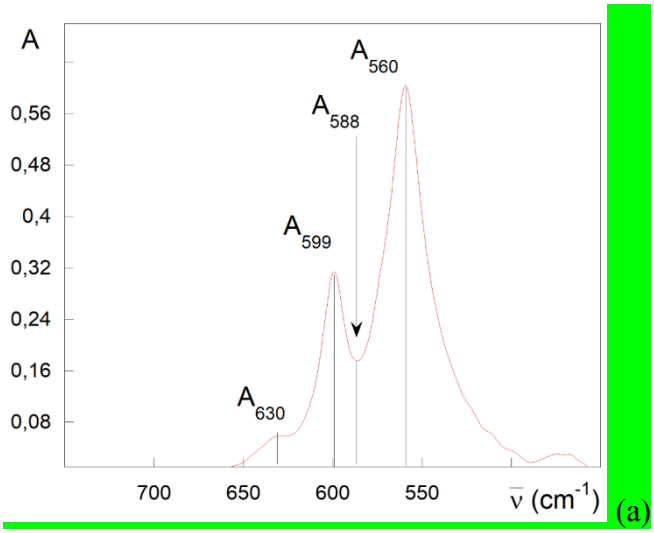

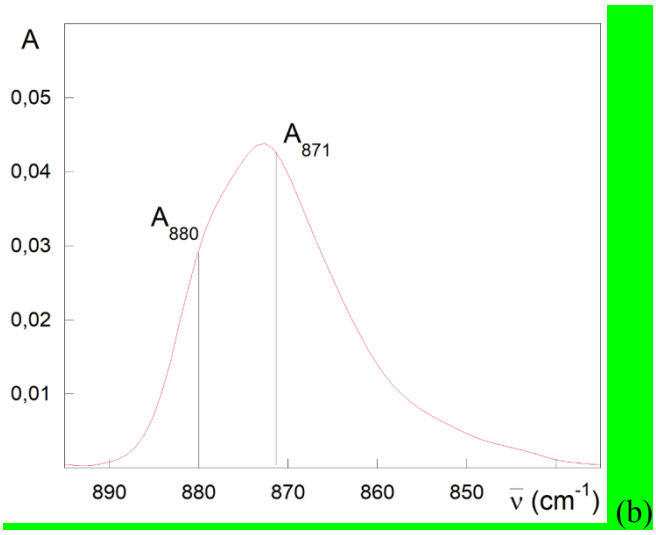

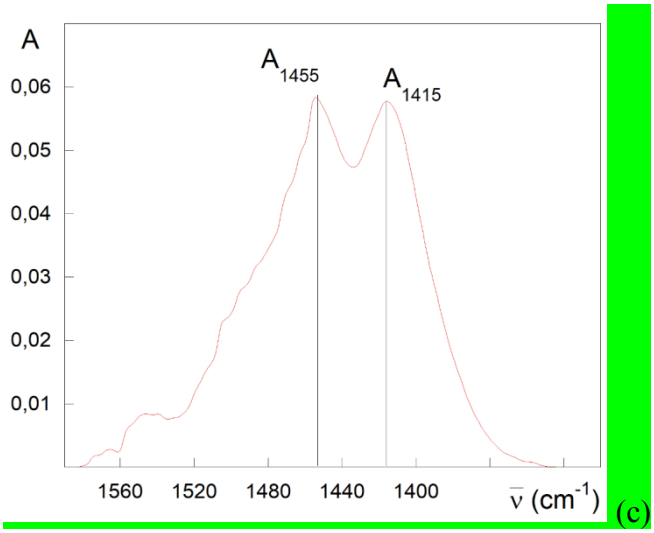

7.3. EPR Analysis

Figure S7. (a) EPR spectra of N1 and orthorhombic fit. Experimental details: modulation amplitude 0.05 mT, time constant 40.96 ms, conversion time 327.68 ms, gain 6.32 10^4, power 2 mW and microwave frequency 9.4239 GHz. Fitting parameters: Lorentzian-type signal, g_1 = 2.0056 (line with H_1 = 0.30 mT), g_2 = 2.0040 (line with H_2 = 0.30 mT) and g_3 = 2.0023 (line with H_3 = 0.34 mT). (b) Isotropic fit for the same experimental spectrum. Fitting parameters: Gaussian-type signal, g = 2.0040 (line with H = 0.52 mT).

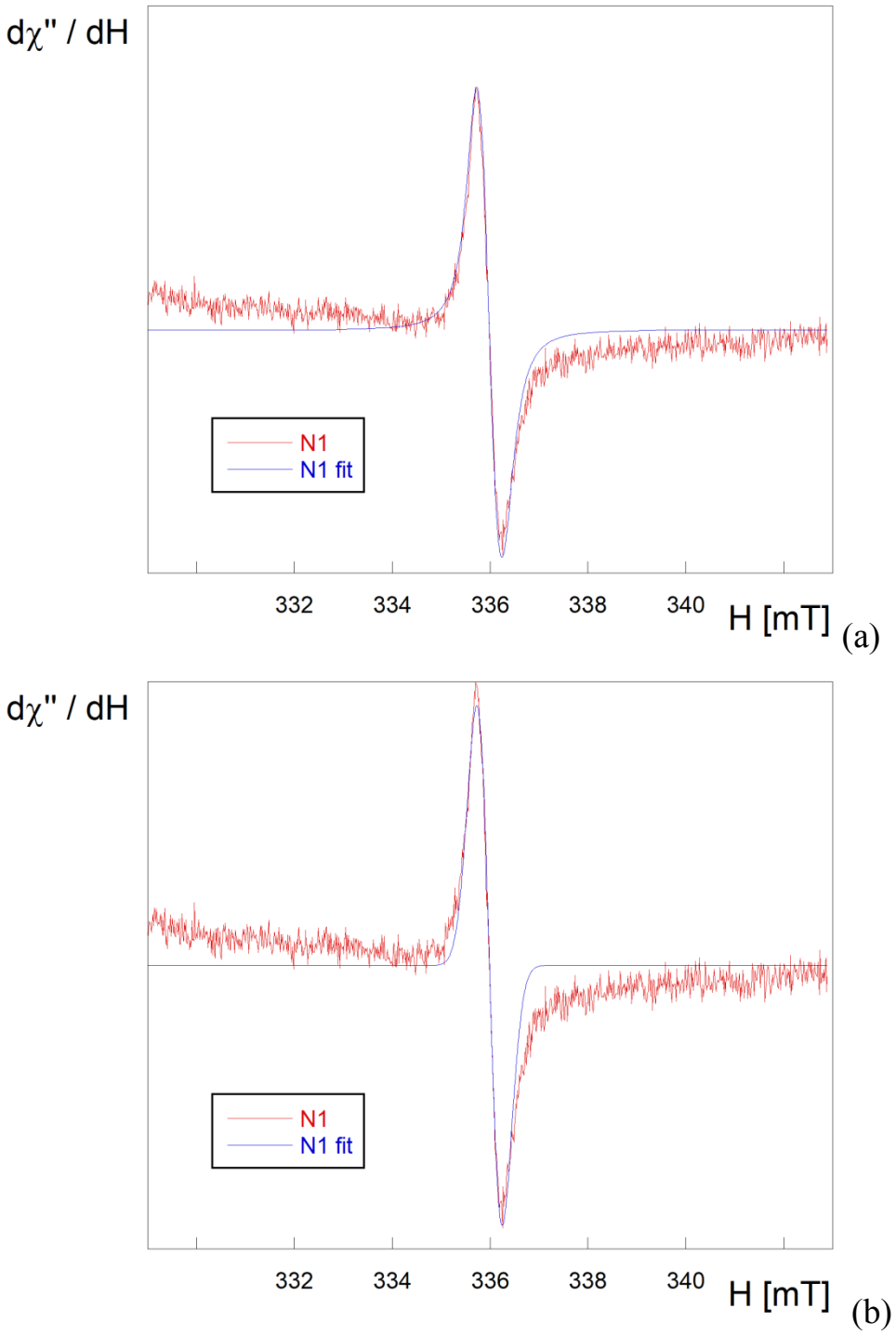

Figure S8. (a) Spectra of F1, N1 and N2 samples. Experimental details given in Figure EPR_1. (b) Spectra of B1 and B2 samples. Experimental details: modulation amplitude 0.1 mT, time constant 40.96 ms, conversion time 327.68 ms, gain 6.32 10^3 and power 20 mW. Microwave frequencies: 9.4242 (B1) and 9.4243 GHz (B2).

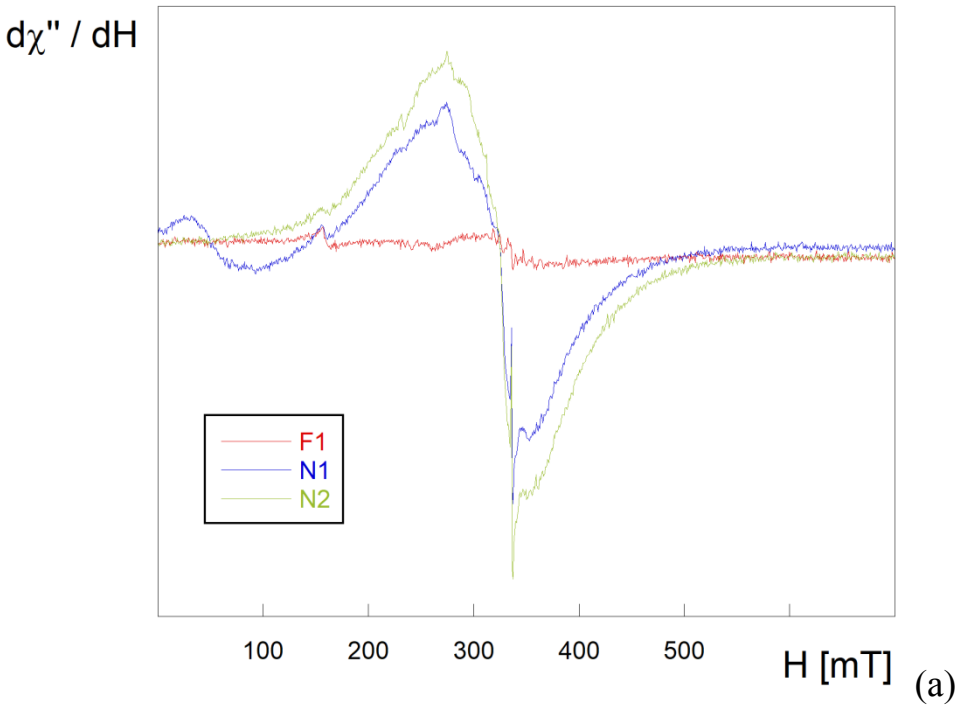

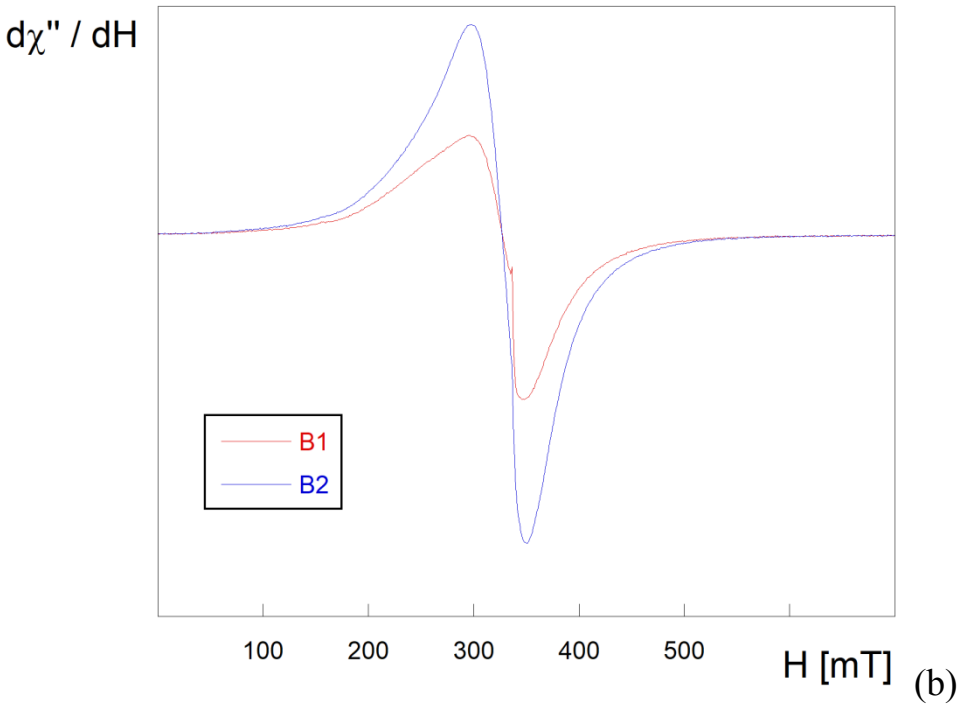

Figure S9. Comparison of the spectra of B1 and synthetic hydroxyapatite. Experimental details: modulation amplitude 0.1 mT, time constant 40.96 ms, conversion time 327.68 ms, gain 6.32 10^4 and power 20 mW. Microwave frequencies: 9.4234 (B1) and 9.4246 GHz (hydroxyapatite).

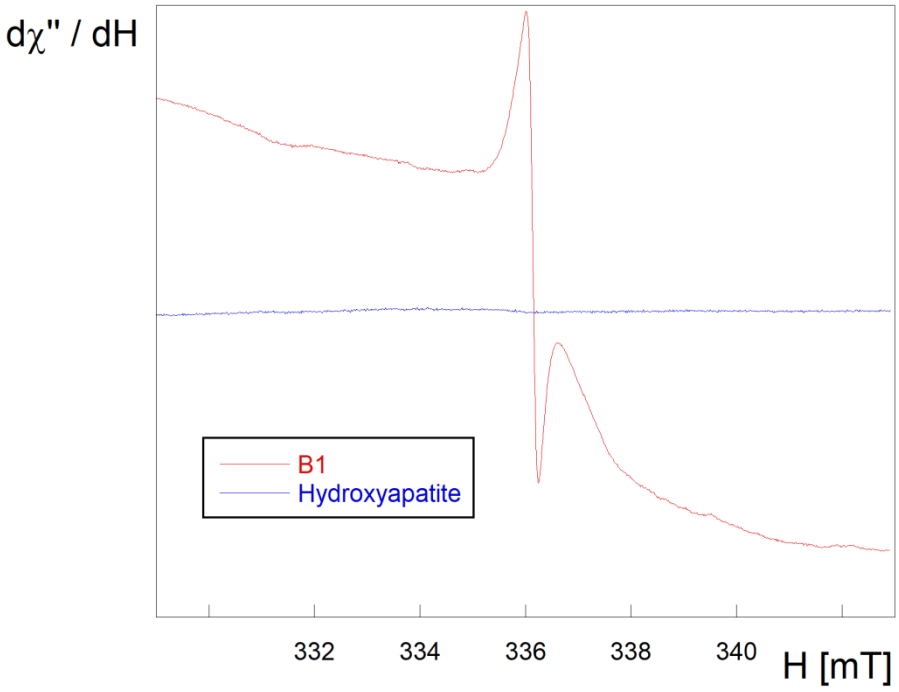
dχ" / dH
B1
Hydroxyapatite
332
334
336
338
340
H [mT]